COST EFFECTIVE SYNTHESIS OF CARBON NANOPARTICLES AND EXPLORING THE FLUORESCENCE AND ELECTROCHEMICAL APPLICATIONS

Synopsis submitted to CHRIST (Deemed to be University)
as partial requirement for the award of the Degree of

DOCTOR OF PHILOSOPHY
IN
PHYSICS

by

ASHLIN M RAJ

Under the Supervision of
Manoj. B
Professor

CHRIST
(DEEMED TO BE UNIVERSITY)
BANGALORE · INDIA

Signature of Scholar **Signature of Supervisor**

CENTRE FOR RESEARCH
CHRIST (Deemed to be University)
BENGALURU

JUNE 2022

CENTRE FOR RESEARCH

Approval of PhD Synopsis

[as per clause 11(k.) of CU Regulation for the Degree of Doctor of Philosophy, May2019]

Name of Scholar:	ASHLIN M RAJ
Department:	PHYSICS AND ELECTRONICS
Name of Co Supervisor:	
Names of Research Advisory Committee: 1. MANOJ B 2. KUNJOMANA A G 3. IMRAN JAFRI R	
Name and Designation of External Reviewer if applicable:	
Date of Synopsis Presentation:	
Title of the PhD thesis:	COST EFFECTIVE SYNTHESIS OF CARBON NANOPARTICLES AND EXPLORING THE FLUORESCENCE AND ELECTROCHEMICAL APPLICATIONS

Approved by:

1. Name of Supervisor: MANOJ B Signature:
2. Name of RAC Member: KUNJOMANA A G Signature:
3. Name of RAC Member: IMRAN JAFRI R Signature:
4. Name of External reviewer if applicable Signature:

Head of Department

Date of approval by Doctoral Committee:

Director Centre for Research

TABLE OF CONTENTS

1. INTRODUCTION 1

2. REVIEW OF LITERATURE AND OBJECTIVES 6

2.1. REVIEW OF LITERATURE 6

2.2. OBJECTIVES 11

3. MATERIALS AND METHODS 12

3.1. FABRICATION OF LUMINESCENT CARBON NANOSTRUCTURES FROM LIGNITE FOR HIGHLY SELECTIVE AND SENSITIVE DETECTION OF COPPER IONS 12

3.2. SYNTHESIS OF FLUORESCENT CARBON NANOSTRUCTURES FROM LIGNITE FOR NON-INVASIVE MICROMOLAR DETECTION AND QUANTIFICATION OF GLUCOSE 13

3.3. PRODUCTION OF CARBON NANOSTRUCTURES FROM LIGNITE FOR SIMULTANEOUS ELECTROCHEMICAL SENSING OF HEAVY METAL IONS CADMIUM AND LEAD 14

3.3.1. Preparation of modified electrode 14

3.3.2. Electrochemical quantification of heavy metal ions cadmium and lead at LA400 modified GCE 14

3.4. CHARACTERIZATION OF THE SYNTHESIZED CARBON NANOSTRUCTURES 15

4. RESULTS AND DISCUSSION 15

4.1. LIGNITE DERIVED FLUORESCENT CARBON NANOSTRUCTURES FOR ULTRASENSITIVE DETECTION OF COPPER IONS 16

4.1.1. Structure and composition of the as-synthesized carbon nanostructures 16

4.1.2. Morphological analysis of the as-synthesized carbon nanostructures 18

4.1.3. Optical behaviour of the as-synthesized carbon nanostructures 20

4.1.4. Analytical application of the as-synthesized carbon nanostructures 23

4.1.5. Conclusion 26

4.2. LIGNITE DERIVED FLUORESCENT CARBON NANOSTRUCTURES FOR NONINVASIVE MICROMOLAR GLUCOSE DETECTION 26

4.2.1. Structure and composition of the lignite derived carbon nanostructures 27

4.2.2. Morphological analysis of the lignite derived carbon nanostructures ... 30

4.2.3. Optical behaviour of the lignite derived carbon nanostructures 31

4.2.4. Efficacy of lignite derived nanocarbon as a glucose sensor 35

4.2.5. Conclusion 41

4.3. LIGNITE DERIVED CARBON NANOSTRUCTURES FOR SIMULTANEOUS ELECTROCHEMICAL SENSING OF HEAVY METAL IONS CADMIUM AND LEAD . 42

4.3.1. Structure and composition of the as-synthesized carbon nanostructures 42

4.3.2. Morphological analysis of the lignite derived carbon nanostructures ... 44

4.3.3. Simultaneous electrochemical sensing of heavy metal ions cadmium and lead using the as-synthesized carbon nanostructures modified glassy carbon electrode 45

4.3.3.1.Repeatability and Reproducibility 52

4.3.3.2.Selectivity and Interference 53

4.3.3.3.Determination of Cd(II) and Pb(II) in real samples 54

4.3.4. Conclusion 55

5. SUMMARY AND FUTURE PROSPECTS 55

6. STRUCTURE OF THE THESIS 57

BIBLIOGRAPHY 58

LIST OF PUBLICATIONS 67

Journal Publications 67

Manuscripts Communicated 67

Patent Communicated 68

LIST OF CONFERENCES AND WORKSHOPS ATTENDED 68

1. INTRODUCTION

In the last three decades, much scientific research has been carried out in the field of carbon nanomaterials all over the world due to their significant electronic, optical, mechanical, chemical, and thermal properties. The zero-, one-, two-, and three-dimensional carbon nanomaterials (i.e., fullerenes (Pang, 1993), carbon nanotubes (Baker & Baker, 2010) , graphene (Zhou et al., 2012), carbon quantum dots (Saikia et al., 2019), carbon nanohorns (Ramya et al., 2016), nanodiamonds (Chang et al., 2007), carbon nanofibres and carbon black) have exhibited such inherent features that can be easily exploited in the development of advanced technology for sensing applications. Furthermore, the employment of nanomaterials within sensors has paved new ways and opportunities to detect analytes or target molecules. For example, carbon nanomaterials-based electrochemical biosensors have reported biocompatibility (Jung et al., 2020), better sensitivity (Huang et al., 2017), better selectivity, and lower detection limits to detect a wide range of chemical to biological molecules.

Carbon precursors and the synthesis method adopted for carbon nanostructures play a pivotal part in feasible large-scale production. Carbon nanostructures have been synthesized using various synthetic approaches from a variety of expensive carbon-based precursors namely, hydrocarbon precursors (Ramya et al., 2016), graphite (Grayfer et al., 2011), carbon black (S. Hu et al., 2009), high grade coal (Moothi et al., 2012), activated carbon (Chingombe et al., 2005), carbon fibre (Treacy et al., 1996), graphite oxide (Kaniyoor & Ramaprabhu, 2012)etc. Synthesis from these carbon-based precursors requires a lengthy extraction process and a high manufacturing cost, which precludes the commercialization of the synthesized carbon nanostructures. Effective utilization of carbon nanostructures in various applications and commercialization depends primarily upon the development of facile, efficient, low temperature, and affordable techniques for large-scale production. Facile production of the carbon nanostructures in an optimal way is possible if one could select abundant, inexpensive precursors with preformed sp^2 domains present in them.

Coal, one of the cheap and abundant naturally occurring materials compared to other derivative source materials, such as graphite, methane, or other hydrocarbons, is a potential source for synthesizing carbon nanostructures. Coal is a carboniferous alluvial rock fuel typically found as deposits or streaks in rock strata (Raj & Balachandran, 2020). It has elemental compositions, such as hydrogen, sulphur,

oxygen, and nitrogen, with a significant presence of other trace elements. Coalification is a biogeochemical process that takes place over an extended period, converting dead plants into peat, which, in turn, transforms to lignite and eventually to anthracite (Y. Zhang et al., 2019). There are abundant nanometer-sized graphitic crystallites within the intrinsic structure of coal that meet the quantum dot size (S. Hu et al., 2016). Coal becomes an ideal carbon source for synthesizing carbon nanostructures if an effective strategy is developed for extracting these domains (S. Hu et al., 2016). The size and shape of the nano-crystallites present in coal depend heavily on the coalification process and its maturity (Saikia et al., 2019). The percentage of sp^2 carbon domain varies with the coalification degree, and the trend is 70, 75, 85, and 94 wt % in lignite, sub-bituminous coal, bituminous coal, and anthracite, respectively (Hoang et al., 2018).

Coal plays a vital role in meeting our society's energy requirements (Raj & Balachandran, 2020). Over a significant period, it is used as a fuel in power plants, transportation, metal refining, textile, and cement production resulting in severe environmental pollution. Coal represents the cheapest natural materials among various precursors because of its abundant reserves. For instance, the coal production globally is over 8 trillion tonnes at ~ 0.05 $/kg, and China affords a production capacity of 1.4 billion tonnes yearly (Su, 2009).

The research community has recognized that the importance of coal extends beyond its use in power production to its conversion into eco-friendly value-added products. The importance of coal as a precursor in the synthesis of carbon nanomaterials has been studied in recent years. The rank of coal has a significant effect on the properties of synthesized carbon nanomaterials (Qin, 2018). Low-grade coal, compared to high-grade coal, is indeed very easy to extract with mild oxidizing agents and produces a high yield (Katalambula & Gupta, 2009; Manoj et al., 2017; Manoj, Raj, & Thomas, 2018; Raj & Balachandran, 2020). Low-grade coals are gaining importance in light of the world's diminishing coal quality. Except for China, approximately 33% of coal produced worldwide is low grade (Raj & Balachandran, 2020). In this context, the different aspects of value addition to low-quality coal are essential.

Lignite is a low-grade coal and low-quality energy source owing to its low energy content with inherent mineral matter compared to other types of coal. It has abundant sp^2 carbon crystallites embedded in its intrinsic 3D matrix, which can be harvested and converted to novel carbon nanostructures in a systematic method. Coal is one of the efficient precursors to synthesize fluorescent carbon nanostructures with

facile synthesis methods, low cost of production (Manoj, Raj, & Thomas, 2018), easy functionalization (Raj & Balachandran, 2020), and high production yield (Raj & Balachandran, 2020). Some of the 0 D fluorescent carbon nanostructures reported from high-rank coal are graphene quantum dots (GQDs) (Y. Zhang et al., 2019); carbon dots (CDs) (Y. Zhang et al., 2019), nanodiamonds (NDs) (Xiao, Liu, & Yang, 2015), etc. They consist of mixed sp^2- and sp^3-hybridized carbon domains and exhibit fluorescence as a result of quantum confinement (Xiao, Liu, & Yang, 2015), functional groups (Hoang et al., 2018), surface/edge state effect, surface state emission mechanisms, etc.

Fluorescence is one of the exciting characteristics of carbon nanomaterials. To date, many carbon nanomaterials with fluorescence properties in the visible region to the infrared region have been synthesized using various synthesis approaches. Fluorescence mechanisms documented thus far to explain the origin of fluorescence in CNs are (1) the effect of quantum confinement given by the carbogenic core (Kumar Thiyagarajan et al., 2016), (2) surface/edge state or defects (Y. Zhang et al., 2019), (3) molecular state (Raj & Balachandran, 2020), and (4) functional groups (Xiao, Liu, Li, et al., 2015). The fluorescence of CNs is dependent upon various factors, such as (1) particle size (Xiao, Liu, Li, et al., 2015), (2) excitation wavelength (Xiao, Liu, Li, et al., 2015), (3) pH (Zhiguo Sun, Xiaoming Li, Ye Wu, Changting Wei, 2018), (4) solvent polarity (H. Wang et al., 2017), (5) surface oxidation degree (Raj & Balachandran, 2020), and (6) surface functionalization (Kumar Thiyagarajan et al., 2016) and heteroatom doping (Yang et al., 2020). Tunable fluorescence is achieved by varying these factors by varying the synthesis approaches. As an alternative mark to fluorophores, such as porphyrins, metal−organic frameworks, DNAzymes, fluorescent aptamers, inorganic quantum dots, for bioimaging and other biomedical applications, fluorescent carbon nanostructures with their reduced cytotoxicity, photobleaching resistance, and improved biocompatibility are of great interest.

However, research on the feasibility of carbon nanostructures as sensors for real-world applications is still in its early stages. Most of the approaches published so far involve a long extraction process, scarce and expensive precursors, and high manufacturing costs, creating a great need for other alternative precursors and techniques.

The first issue dealt with in the current study is the metal ions contamination in the environment. Metal ions contamination is the leading cause of many health and environmental problems (Anas et al., 2019). In order to rectify and remediate the

environment from metal ions contamination, simple, efficient, and easy to fabricate sensors for the on-site detection of metals ions is obligatory. Copper is third in abundance (after iron and zinc) among the essential transition metal ions in the human body and plays a vital role in various physiological processes. Many proteins contain copper ions in the catalytic center. Copper ions also catalyse the formation of reactive oxygen species (ROS) that can damage lipids, nucleic acids, and proteins (Xu et al., 2018). Several studies have related the cellular toxicity of copper ions to serious diseases, including Alzheimer's disease, Indian childhood cirrhosis (ICC), prion disease, and Menkes and Wilson diseases (Jayaweera et al., 2019). Due to the extensive use of copper in modern society, copper ions have also become a significant metal pollutant (G. Wang et al., 2014). The limit of copper in drinking water as set by the US Environmental Protection Agency (EPA) is 20 μM (1.3 ppm).

The second issue dealt with in the current study is developing a non-invasive and cost-effective glucose-sensing technique for improved management of diabetes. Diabetes and various malignancies have been linked to the breakdown of glucose transport in the human body. Therefore, one of the crucial aspects of biomedical surveillance and diagnosis (W. Zhang, Du, et al., 2015) is the accurate monitoring of glucose concentrations. Since glucose is the primary energy source for cells, it is involved in an extensive range of metabolic processes, either actively or passively. The standard medical procedure monitors blood or plasma glucose levels using a handheld glucose meter or more advanced laboratory instrumentation (Yoo & Lee, 2010). At present, commercial glucometers provide only invasive, non-real-time measurements (Danielle Bruen, Colm Delaney, 2017). There is a requirement for non-invasive, real-time, and highly efficient glucose detection devices. The potential to test blood glucose without a needle and with little or no discomfort has been one of the ultimate goals of diabetes research. Without discomfort and disruption to the skin, conformity with glucose testing and monitoring will significantly improve. This will ultimately result in improved management of diabetes and its complications. The synthesis and surface modification of fluorescent nanomaterials have been well established in the laboratory; however, mass production of nanostructures has not been fully achieved, posing a significant barrier to the development of nanostructured glucose biosensors with high sensitivity and excellent selectivity, as well as other applications.

The third issue dealt lead in the current study is the contamination of water by heavy metals, which is one of the significant issues to be faced throughout the world

and requires special attention. Population growth, industrialization, and urbanization have contributed to freshwater depletion (Anas et al., 2019), creating a severe shortage of safe drinking water in several regions across the globe. Water scarcity, combined with discharges of hazardous industrial effluents into bodies of water, demands highly efficient wastewater decontamination technologies. Heavy metal ions such as cadmium and lead are among the most prevalent metal pollutants affecting the aquatic environment worldwide (Rahman, 2017; Wei et al., 2012). Cadmium and lead are extensively employed in the mining, leather, metal plating, tanning, semiconductor manufacturing, production lines, printing, textiles, dyes, etc. According to the U. S. Environmental Protection Agency (EPA), the maximum permissible limit of cadmium is 5 ppb and lead is 10 ppb (Rahman, 2017; Wei et al., 2012), and above this concentration, it is harmful to ecology. Thus, the excess release of cadmium and lead contaminates the environment, disturbs the ecosystem, and shows serious adverse effects on humans, flora, and fauna. The abnormal doses of cadmium and lead can cause renal abnormalities, lung cancer, bones demineralization, breast cancer, etc. Moreover, the regular inhalation of cadmium and lead can result in fever, edema, or even death. Thus, due to these serious consequences of excess cadmium and lead contamination, a qualitative and quantitative estimation of cadmium and lead in the environment is essential.

Electrochemical techniques have been recognized as promising for highly sensitive, on-site analysis of heavy metal ion concentrations due to the simple, fast, portable, and inexpensive equipment required (Rahman, 2017; Wei et al., 2012). Indeed, electro analytical stripping techniques, including anodic stripping voltammetry, cathodic stripping voltammetry, and potentiometry, have been identified as promising metal-ion detection methods due to their intrinsic sensitivity and selectivity. Among them, square-wave stripping voltammetry (SWSV) is the most sensitive technique for trace analysis of heavy metals (Rahman, 2017; Wei et al., 2012).

Recently, because of the large surface area and nano-scale properties, carbon nanomaterials have been used as promising electron mediators to modify the electrodes for electrochemical sensing applications. Due to the exotic properties of carbon nanomaterials and the possibilities of their modifications with different functional groups, the electrochemical sensors based on carbon nanomaterials achieve high sensitivity and specificity, enhanced conductivity, and the lowest detection limit with less response time. However, literature revealed that minimal work had been done on

the electrochemical sensing of cadmium and lead using modified electrodes. The present work deals with the multiple utility of lignite derived nanocarbon in fluorescent and electrochemical sensing application.

2. REVIEW OF LITERATURE AND OBJECTIVES

2.1. REVIEW OF LITERATURE

Synthetic methods of carbon nanostructures can be generally classified into two main categories: top-down and bottom-up methods. Top- down methods carry out the cleavage or breaking off of carbon precursors to produce carbon nanostructures, and bottom-up methods build carbon nanostructures from molecular precursors (Rahman, 2017; Wei et al., 2012).

Characteristics of precursors, mainly carbon content, carbon-chain length, functional groups, etc., play a vital role in the structure and properties of carbon nanostructures (Saikia et al., 2019). The unique chemical structure of coal bestows added benefit over pure sp^2-hybridized carbon, such as graphite, because it has disordered configuration and small crystalline carbon domains joined by weak carbon chains (Raj & Balachandran, 2020). This chemical structure provides easy dispersion, extraction using mild chemicals, functionalization oxidative scissoring, and low-toxicity nature for coal, whereas large graphite structures need stronger oxidizing agents, such as $KMnO_4$ with H_3PO_4 and H_2SO_4, for the extraction process (Y. Wang & Hu, 2014).

The viability of producing carbon nanostructures from coal was first discovered after (Pang, 1993) synthesized fullerene from Australian coke. Since then, coal of different ranks has been explored for the synthesis of a diverse class of carbon nanostructures, such as graphite (Rodrigues et al., 2011), activated carbon (Rodrigues et al., 2011), carbon nanotubes (Rodrigues et al., 2011), carbon nanospheres (Manoj, Raj, & Chirayil, 2018), graphene oxide (Hoang et al., 2018), graphene (Savitskii, 2017), porous carbon (Bijiang Geng, Dewen Yang, Fengfeng Zheng, Chen Zhang, Jing Zhan, Zhen Li & Wang, 2017), GQDs (Kovalchuk et al., 2015), CDs (M. Li et al., 2017), NDs (Xiao, Liu, & Yang, 2015), etc. Fluorescent carbon nanostructures from coal are synthesized using various top-down techniques, such as oxidation reaction using concentrated H_2SO_4 and HNO_3 (Manoj, Raj, & Thomas, 2018), H_2O_2 (Saha & Sarkar, 2019), a combined method of carbonization (at different temperatures) and acidic

oxidation (Saikia et al., 2019), etching (Ye et al., 2015), laser ablation technique (Xiao, Liu, & Yang, 2015), cross-flow ultrafiltration technique (Ye et al., 2013) along with varying the oxidation temperature (Lueking et al., 2007), refluxing in ethylenediamine solution (Kumar Thiyagarajan et al., 2016), microwave irradiation (Kumar Thiyagarajan et al., 2016), solvothermal treatment in toluene (Bijiang Geng, Dewen Yang, Fengfeng Zheng, Chen Zhang, Jing Zhan, Zhen Li & Wang, 2017) and dimethylformamide (DMF) (M. Li et al., 2017), low-power ultrasound (M. Li et al., 2017), acid/ultrasonic mixed oxidation technique (Saikia et al., 2019), green ozone oxidation (Liu, Xuexia , Hao, a, Jianhui Liu, b, 2018), ultrasonic- assisted wet-chemical method (Saikia et al., 2019), ultrasonic cell crusher (K. Li et al., 2017), acoustic cavitation (C. Hu et al., 2014), etc. The properties of the carbon nanostructures synthesized from coal depend upon various factors, such as the rank of coal, carbonization temperature, degree of oxidation, reaction time, reaction temperature, etc (Raj & Balachandran, 2020).

The chemical oxidation method is one of the facile and effective methods for the extraction of carbon nanostructures from coal. The small-sized crystalline carbon domains with defects present in the coal can be easily displaced with a simple oxidation technique. This method introduces negatively charged oxygen functional groups to the synthesized carbon nanostructures, making them hydrophilic and defective in nature (Raj & Balachandran, 2020). Ye et al. (Ye et al., 2015) reported the synthesis of different ranks, anthracite, bituminous coal, and coke, using a one-step acidic oxidation technique with H_2SO_4 and HNO_3. The morphologies of the three types of GQDs were different originating from the different structure of coals. These GQDs also showed stable size-dependent and pH-dependent fluorescence in aqueous solutions. Hu et al. (S. Hu et al., 2016) explained the formation mechanism of CDs from anthracite coal using a green oxidizing agent H_2O_2. This approach introduces a synthesis method, which does not incur the burden of toxic gas emission. The coal samples were ball-milled initially, which led to an increase in their specific surface area, which, in turn, resulted in complete contact with the H_2O_2 reactant. Here, active OH radicals present in H_2O_2 are used for the removal of organic carbon chains by oxidation of these into carbon dioxide (CO_2) and water (H_2O) along with heating, which leaves behind a stable crystalline carbon domain. Dong et al. (Dong et al., 2014) explored six coals of varying ranks for the synthesis of CDs using acidic oxidation followed by the centrifugation technique. The obtained GQDs show excitation-dependent fluorescence and excellent

electrochemiluminescence properties. The production yield of GQDs was revealed to be obviously dependent on the rank of coal. It decreased from 56.30% to 14.66% as the rank of the six investigated coals gradually increased. In addition to GQDs, some other carbon nanostructures such as GO, CQDs, agglomerated GQDs and agglomerated CQDs could also be found in coal, indicating that coal may also be used to prepare these carbon nanostructures.

The rank of coal is one of the crucial factors controlling the characteristics of the synthesized carbon nanostructures. A coal structure study showed that low- and medium-ranked coal comprised more functional groups (Raj & Balachandran, 2020), side chains, bridge bonds, hydrogen bonds, and loose structures, with few layers and small aromatic rings (Qin, 2018). As the rank of coal falls, the dense carbon ring structure of coal-based GQDs loosens the hexagonal structure and the content of sp^2 carbons becomes less, producing a vacancy defect (W. Zhang, Jiang, et al., 2015). Low-grade (low-quality) coals are becoming increasingly important in light of the declining coal quality around the world.

Copper ion, significantly, plays a critical role in the areas of environmental, biological and chemical systems. It is an essential trace element for both plants and animals, including humans. The U.S. Environmental Protection Agency (EPA) has set the limit of copper in drinking water to be 20 μM (1.3 ppm) (Shi et al., 2020). Also, the average concentration of blood copper in the normal group is 100–150 g dL^{-1} (15.7–23.6 M) (M. Li et al., 2014). However, exposure to high level of copper even for a short period of time can cause gastrointestinal disturbance, while long-term exposure causes liver or kidney damage (M. Li et al., 2014). Thus, it is desirable to have a reliable and sensitive analytical method to qualify and quantify the level of Cu(II) ions present in the environment and the ecosystem. By now, many methods have been proposed for the determination of copper ions, including fluorescent-probe sensors based on organic dyes/organic complex (M. Li et al., 2014), carbon dots (Ruedas-rama et al., 2013), CdSe–ZnS SQDs (Sung & Lo, 2012), etc., and other methods such as atomic absorption spectrometry (Rahman, 2017), inductively coupled plasma mass spectroscopy (Wei et al., 2012), and electrochemical methods (Ramdass et al., 2017). In summary, despite the aforementioned methods, most of the reported methods require relatively high cost apparatus, sophisticated and time-consuming procedures, even with partial toxic reagents. Therefore, it is highly necessary to develop a promising method for simple,

low-cost and rapid tracking of Cu^{2+} ions in biological, toxicological, and environmental samples to overcome most of these difficulties.

Hu et al. (C. Hu et al., 2014) demonstrated Cu^{2+} sensing using anthracite coal based carbon nanostructures produced by the acidic oxidation method. The CDs contained N and O chelate groups on the surface, resulting in fast metal−ligand kinetics. Because copper ions have a high thermodynamic affinity toward N and O chelate groups, copper ions could quench the fluorescence of CDs up to a concentration of 2 nm.

Diabetes is a metabolic disorder, indicated by blood glucose concentrations, and causes with long-term damage and failure of various organs like the heart, kidney, eyes, and blood vessels (Chen et al., 2013). The early and sensitive detection of abnormal glucose level in the blood is very important for proper treatment to reduce many health problems (Choudhary et al., 2014; P. Zhang et al., 2015). One important method is utilizing the enzyme glucose oxidase (GOx). H_2O_2 is the main product of the glucose oxidase (GOx)-catalyzed oxidation of glucose in the presence of oxygen(Yi et al., 2013). In this way, the concentration of glucose can be determinated by monitoring the production of H_2O_2.

Currently, the available glucose detection process employs a glucose oxidase/dehydrogenase biosensor device (Chansaenpak et al., 2021; Ferri et al., 2011; Mano, 2019; Yoo & Lee, 2010). These enzyme biosensors function remarkably well in the millimolar concentration of blood/plasma glucose. Certain applications specifically test the fluorescence of the enzyme cofactor, while others make use of quantum dots to mark the cofactor. Unfortunately, when concentrations reach micromolar levels, sensor fabrication becomes more complex and production costs high. Since glucose concentrations in noninvasively extracted biofluids are typically in the micromolar scale, detection techniques capable of measuring glucose at these concentrations are essential.

Carbon nanomaterials, such as, graphene, carbon nanotubes (CNTs), crystalline diamond, and diamond-like carbon display exceptional electrochemical properties which have resulted in their widespread application(Mendes et al., 2018; Petit & Puskar, 2018; Shinde & Pillai, 2012). The potential of these materials is unquestionable in sensing applications, as the novel carbon-derived nanomaterials possess properties that are unfathomable in bulk materials. This results in their capability to operate with not only a higher sensitivity and selectivity in harsh environments but also over greater

temperature and dynamic ranges. Historically, a number of materials including platinum, gold, and various forms of carbon have been exploited as electrode materials for electrochemical detection. Graphene, CNTs and diamond are the polymorphs of carbon that have been widely employed as electrode materials for electrochemical sensing in recent years (Awasthi et al., 2015; Shuvo et al., 2013).

Heavy metals such as cadmium and lead pose a detrimental risk to human health and the environment due to their toxicity; even exposure to minuscule quantities can be life threatening (Jaishankar et al., 2014). Accordingly, exploring the sensitive, rapid and simple analytical method for precise monitoring of Pb^{2+} and Cd^{2+} is urgently needed. The usual methods adopted for the concentration assessments of the metal ions are mainly focused on the use of atomic absorption or inductively coupled plasma (ICP) atomic emission spectroscopy, ICP-mass spectrometry and electrochemical (EC) techniques. However, spectroscopy methods are somewhat cumbersome and not suitable for the in situ measurement due to the ponderous and complicated instruments. On the contrary, EC techniques have attracted growing interests due to high-sensitivity, portability and low cost. Among all the EC methods, electrochemical stripping voltammetric analysis provides a powerful tool for the determination of metal ions (Wei et al., 2012), which possess high-sensitivity for the metal analysis due to the built-in preconcentration step and is very suitable for on-site and in situ analysis. Most commonly used, mercury-based electrodes including hanging drop mercury electrode and mercury film electrodes are adopted because of excellent reproducibility and high-sensitivity (Wei et al., 2012). However, due to the dramatic toxicity of mercury, numerous attempts have been made to replace it with new mercury-free and reliable electrode. Recently, the bismuth film electrode (BFE) has drawn the increasing attentions in the field of the stripping technique due to the remarkably low toxicity and the ability to form alloy with many metals as well as its wide potential window, which has proved to be equal to or even superior to that of MFEs (Rahman, 2017; Shi et al., 2020). On the other hand, in order to alleviate interferences and improve the sensitivity of the sensing interface, some strategies have also been exploited for the stripping analysis, such as, the chemical modified electrode (CME), heated electrodes, microwaved electrodes, and insonated electrode. Among these, CME capable of accumulating target analytes from dilute aqueous solution has been developed as the fascinating and effective way for the anodic stripping voltammertry (ASV) determination of heavy metal ions. Prominent examples include functionalized

mesoporous silica electrode (Dai et al., 2014), carbon nanotubes (CNT) modified electrode (Jahandari et al., 2013), ordered mesoporous carbon (Zhu et al., 2008), acetylene black paste electrode (G. Li et al., 2006), nanocrystalline diamond thin-film electrode (Sonthalia et al., 2004), and thick film modified graphite-containing electrode (Brainina et al., 2004). Although all the above material showed improved stripping signals, especially the CNT modified electrode, new materials are still needed to develop highly sensitive and antifouling metal ions sensing platform.

In contrast to the widely studied world of synthetic carbonaceous materials, the optical and electrochemical properties (and corresponding range of tunability) of natural carbonaceous materials are still poorly understood. Yet, this gap in understanding is worth bridging, particularly given the massive global availability of low cost naturally formed carbonaceous materials (take coal as an example: nearly 8 gigatonnes per year produced globally at ~ 0.05 $/kg). Such materials may find uses beyond combustion, in many of the applications in which synthetic carbon materials are currently being deployed. Due to the wide array of molecular compounds present in different natural carbonaceous materials (from aromatic to aliphatic, with a varying degree of functional chemistry), these materials could provide a broad range of optical and electrochemical properties at extremely low cost. In order to unlock the potential of these materials, it is crucial to develop compatible, low-cost methods of processing them, characterize the as-synthesized carbon nanostructures, and measure their optical and electrochemical characteristics. There is a dearth of explicit research on these carbon nanostructures for their facile and low-cost scalable synthesis and affordable practical applications in everyday life to address significant social issues.

Accordingly, the research work presented herein would focus on the simple, economical, and scalable synthesis of carbon nanostructures from low grade coal, lignite. In addition, three critical issues confronting our society at the moment: copper pollution in water, development of non-invasive and cost-effective glucose-sensing technique, and contamination of water by heavy metals, would be addressed by the synthesized carbon nanostructures.

2.2. OBJECTIVES

The present study aims for the beneficiation and value addition of low-grade Indian coal into high-value materials like carbon nanostructures for the most demanding

real-world applications in the healthcare, and environmental sectors, with the following objectives.

- To fabricate luminescent carbon nanostructures from low grade coal for ultrasensitive detection of copper ions.
- To fabricate luminescent carbon nanostructures from low grade coal for non-invasive micromolar glucose detection.
- To utilize the as-synthesized carbon nanostructures for the simultaneous electrochemical sensing of heavy metal ions cadmium and lead.

3. MATERIALS AND METHODS

3.1. FABRICATION OF LUMINESCENT CARBON NANOSTRUCTURES FROM LIGNITE FOR HIGHLY SELECTIVE AND SENSITIVE DETECTION OF COPPER IONS

About 5 g of the powdered lignite was oxidized using 100 mL dilute HNO_3 (Water: HNO_3: 5:1) followed by repeated washing with deionized water. Further, it was sonicated for 1 hour followed by magnetic stirring at a temperature of 100 °C (1 hour). The obtained sample was reduced to a pH of 7.7 using NaOH (4 g NaOH in 100 mL H_2O). This was followed by magnetic stirring without heating for 1 hour. Further, the sample was centrifuged at 12,000 rpm for 30 minutes. After centrifugation, the sample was separated out as residue (LC1-yield of 1.3 g) and supernatant. The supernatant was filtered through a dialysis membrane retaining the large particles inside the membrane (LC2-yield of 0.9 g). The remaining permeate which are the smaller particles (LC3-yield of 1.7 g) were collected outside the membrane separately. All the three samples (LC1, LC2 and LC3) were dried by slow evaporation at 80°C. The combined production yield of the nanostructure is found to be 78% which is very high production yield for gram scale production of fluorescent graphene quantum dots.

The obtained products LC1, LC2 and LC3 were refluxed and sonicated in chloroform and products were dried out and labelled as LC1C, LC2C and LC3C respectively.

The utility of the synthesized nanocarbon as a fluorescent sensor for detection of metal ions was performed at room temperature in PBS (pH 7.0) buffer. Potassium (K^+), calcium (Ca^{2+}), magnesium (Mg^{2+}), ferrous (Fe^{3+}), chromium (Cr^{2+}), nickel

(Ni^{2+}), zinc (Zn^{2+}), lead (Pb^{2+}), sodium (Na^{+}), manganese (Mn^{2+}) and copper (Cu^{2+}) solutions were prepared with a concentration of 30 ppm. 100 µL of each metal ion solution was added separately to 1000 µL PBS buffer. Three samples LC1, LC2 and LC3 (2.2 μgmL^{-1}) were added separately to each buffer-ion solution. The fluorescence emission spectrum was noted after shaking the mixture for 5 seconds at RT. The copper ion selective quenching of LC3 at different pH conditions (acidic to alkaline) was investigated. To test the feasibility of the sensors, spiked samples were prepared by combining three different concentrations of copper ions into the lake water and tap water samples.

3.2. SYNTHESIS OF FLUORESCENT CARBON NANOSTRUCTURES FROM LIGNITE FOR NON-INVASIVE MICROMOLAR DETECTION AND QUANTIFICATION OF GLUCOSE

5g of lignite coal was finely ground using a motor pestle. The obtained lignite powder was refluxed with 100 ml nitric acid in water: HNO_3 ratio of 5: 1 followed by magnetic stirring for 1 hour. Followed by centrifugation for an hour at 12000 rpm, the residue was separated and dried. The obtained dried residue was divided into three parts, and each part was heated to a different temperature (100°C, 150°C and 200°C). The final products were designated as LR100, LR150 and LR200.

All of the fluorescence spectra were recorded on a fluorescence spectrophotometer. The emission spectra were recorded under a fixed excitation wavelength of 485 nm. For the study of the quenching effect of glucose on as-synthesized carbon nanostructures, 30 µL of glucose oxidase (GO_x) (0.2 mg/mL) was mixed with 400 µL carbon nanostructures solution, then the glucose solutions with different concentrations (8-3000 µM) were added into the carbon nanostructures/GOx mixture, and then the mixed solution was diluted with DMF to 600 µL (pH- 6.3). The mixture was shaken for a minute and measured by using fluorescence spectrophotometer at RT. To investigate the selectivity of fluorescence quenching of the synthesized nanocarbon materials towards glucose, solutions of common interference species, namely dopamine, uric acid, ascorbic acid, K^{+}, Ni^{2+}, Ca^{2+}, Mg^{2+}, Fe^{3+}, Na^{+} and Mn^{2+} (30 µM), were prepared in PBS (pH=7). Each interferent was added individually to the specific nanocarbon (25 µg/ml) in 100-fold and mixed thoroughly.

To test the feasibility of the sensors, spiked samples were prepared by combining three different concentrations of glucose into the diluted human urine and saliva samples.

3.3. PRODUCTION OF CARBON NANOSTRUCTURES FROM LIGNITE FOR SIMULTANEOUS ELECTROCHEMICAL SENSING OF HEAVY METAL IONS CADMIUM AND LEAD

5g of lignite coal was finely ground using a motor pestle. The obtained lignite powder was refluxed with 300 ml nitric acid in water: HNO_3 ratio of 5: 1 followed by magnetic stirring for 2 hours at 800 rpm. The solution was dried at 100°C along with stirring followed by heating at a temperature of 400°C. The obtained product was labelled as LA400.

3.3.1. PREPARATION OF MODIFIED ELECTRODE

Ultrasonic agitation (for 5 min) was used to disperse LA400 into alcohol to give a suspension. Prior to the surface modification, the bare glassy carbon electrode (GCE) was polished carefully with 0.05 μm alumina powder and rinsed with DI water, followed by being sonicated in alcohol and DI water successively and dried under lamp. The prepared material and Nafion (5 wt %) were taken in the ratio 10:1 and dispersed in N-Methyl-2-pyrrolidone (NMP) via sonication. An aliquot of 10 μL of the mixture was coated on glassy carbon electrode, and then the solvent was evaporated at room temperature to obtain the LA400 modified electrode.

3.3.2. ELECTROCHEMICAL QUANTIFICATION OF HEAVY METAL IONS CADMIUM AND LEAD AT LA400 MODIFIED GCE

The electrochemical measurements were performed with LA400 modified glassy carbon as the working electrode, Ag/AgCl , and platinum wire as reference and counter electrode respectively in 1 M HCl as the electrolyte. Square wave anodic stripping voltammetry (SWASV) was used for the detection under optimized conditions. Cd and Pb were deposited at the potential of -0.7 V for 50 s by the reduction of Cd (II) and Pb (II) in 1 M HCl. The anodic stripping (reoxidation of metal-to-metal ions) of electrodeposited metal was performed in the potential range of -1.1 to -0.3 V at the following parameters: frequency, 15 Hz; amplitude, 25 mV; increment potential, 4 mV. The simultaneous and selective detection of Cd (II) and Pb (II) has been performed at the same experimental condition.

The reproducibility and repeatability of LA400 modified GCE electrode for Cd (II) and Pb (II) determination were tested in 24 nM cadmium and lead ion solution. The

selectivity of LA400 modified GCE electrode towards Cd (II) and Pb (II) sensing was examined by studying the effect of closely associated interfering substances such as potassium (K^+), nickel (Ni^{2+}), calcium (Ca^{2+}), magnesium (Mg^{2+}), ferrous (Fe^{3+}), sodium (Na^+), manganese (Mn^{2+}), mercury (Hg^{2+}), and copper (Cu^{2+}) were added in 100-fold concentrations in the determination of 24 nM Cd (II) and Pb (II) in PBS (pH 7.0). For real-sample analysis, three different concentrations of Cd (II) and Pb (II) ions were prepared. All the sensing experiments were repeated thrice to ensure reproducibility.

3.4. CHARACTERIZATION OF THE SYNTHESIZED CARBON NANOSTRUCTURES

High-Resolution Transmission Electron Microscope (HRTEM) images were captured using Jeol/JEM 2100. The Fourier Transform Infrared (FTIR) spectrum was acquired using a Thermo Nicolet-Avtar 370 spectrometer. Elemental analysis of the samples was performed on the Elementar Vario EL111 elemental analyzer (CHNS). Raman spectrum was obtained using a Horiba LabRAM HR spectrometer. UV/Vis spectrometer (Ocean optics JAZ series) and Shimadzu spectrofluorometer (RF5301PC) were used to obtain absorption and fluorescence spectral measurements. The HORIBA Fluorolog FL-1057 spectrometer (TCSPC) was used to determine the fluorescence lifetime.

Deionized water was used throughout the experiments. All the experiments were repeated thrice to ensure reproducibility.

4. RESULTS AND DISCUSSION

The present work outlines a) the feasibility of synthesizing carbon nanostructures from low-grade coal-lignite using facile and inexpensive techniques that could open up the possibility of mass production of carbon nanostructures on an industrial scale, b) investigating the role of dialysis separation on the structure, composition, morphology and optical characterizations of carbon nanostructures c) investigating the role of synthesis temperature on the structure, composition, morphology and optical characterizations of carbon nanostructures d) utilizing the fluorescence property of the as-synthesized carbon nanostructures for the sensing of

copper ions and glucose molecules and electrochemical property sensing for the sensing of heavy metal ions cadmium and lead.

4.1. LIGNITE DERIVED FLUORESCENT CARBON NANOSTRUCTURES FOR ULTRASENSITIVE DETECTION OF COPPER IONS

In the current study, carbon nanostructures (LC1, LC2, and LC3) of different structure, composition, morphology and optical characterizations are synthesized utilizing dialysis separation from low-grade coal lignite and the as-synthesized carbon nanostructures are utilized for the fluorescence sensing of copper ions.

4.1.1. Structure and composition of the as-synthesized carbon nanostructures

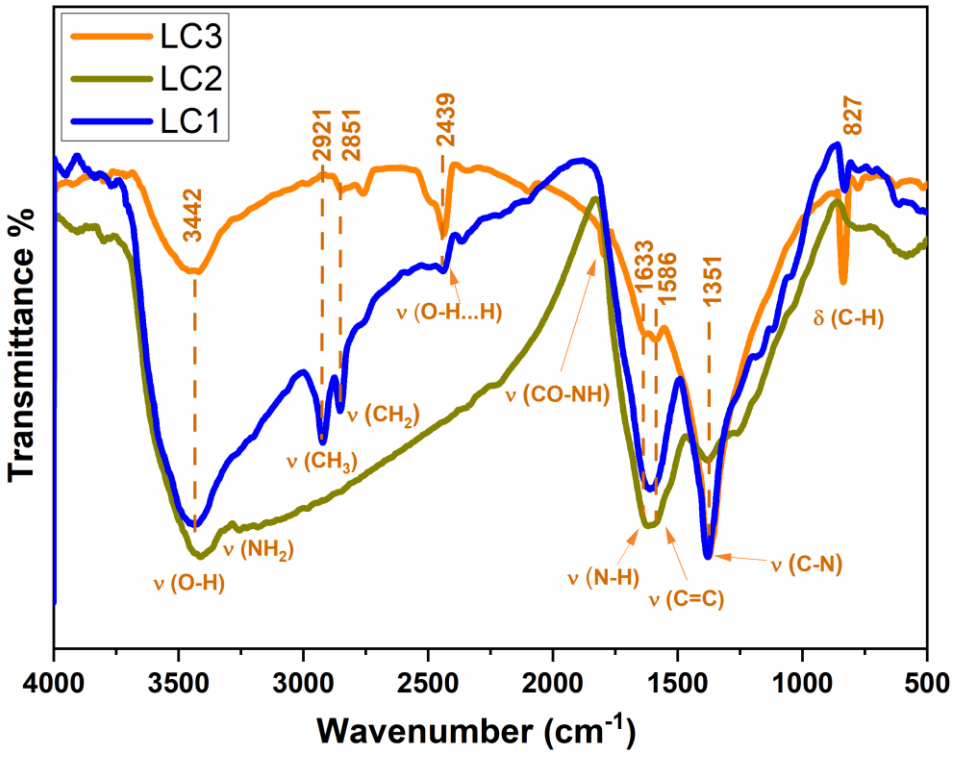

Figure 1: FTIR spectra of carbon nanostructures LC1 (residue), LC2 (sample inside the dialysis membrane) and LC3 (permeate outside the dialysis membrane)

The obtained carbon nanostructures were characterized by fourier transform infrared spectroscopy (FTIR) (Figure 1). The spectra have prominent bands at 1633 cm^{-1}, 1351 cm^{-1}, 2851 cm^{-1}, 2922 cm^{-1}, 2439 cm^{-1}, and 3200-3500 cm^{-1}. The band at 1633 cm^{-1} is originated from the N-H stretching present in the nanocarbon. The 1351 cm^{-1} band is due to – C-N stretching, and the band at 2921 cm^{-1} in LC1 arises from the - CH_3 stretching. The peak at 2851 cm^{-1} in LC1 and LC3 is ascribed to - CH_2 stretching.

The 2439 cm^{-1} peak in LC1 and LC3 originates from the stretching vibration of H-bonded O-H (carboxylic acid). The (3200-3500) cm^{-1} band arises from the O–H stretching (adsorbed water, hydrogen-bonded hydroxyl) and NH_2 stretching (Balachandran, 2014). The relative peak intensities of O-H stretching vibration and stretching vibration of H-bonded O-H (carboxylic acid) are much stronger for LC2 than those for LC3. From this fact, we speculate that there are more –OH and –COOH functional groups present in the product inside the dialysis membrane. The FT-IR analysis confirms that the synthesized product contains an abundant graphitic structure with hydroxyl and carboxyl functional groups which makes it highly soluble and form a stable suspension in water.

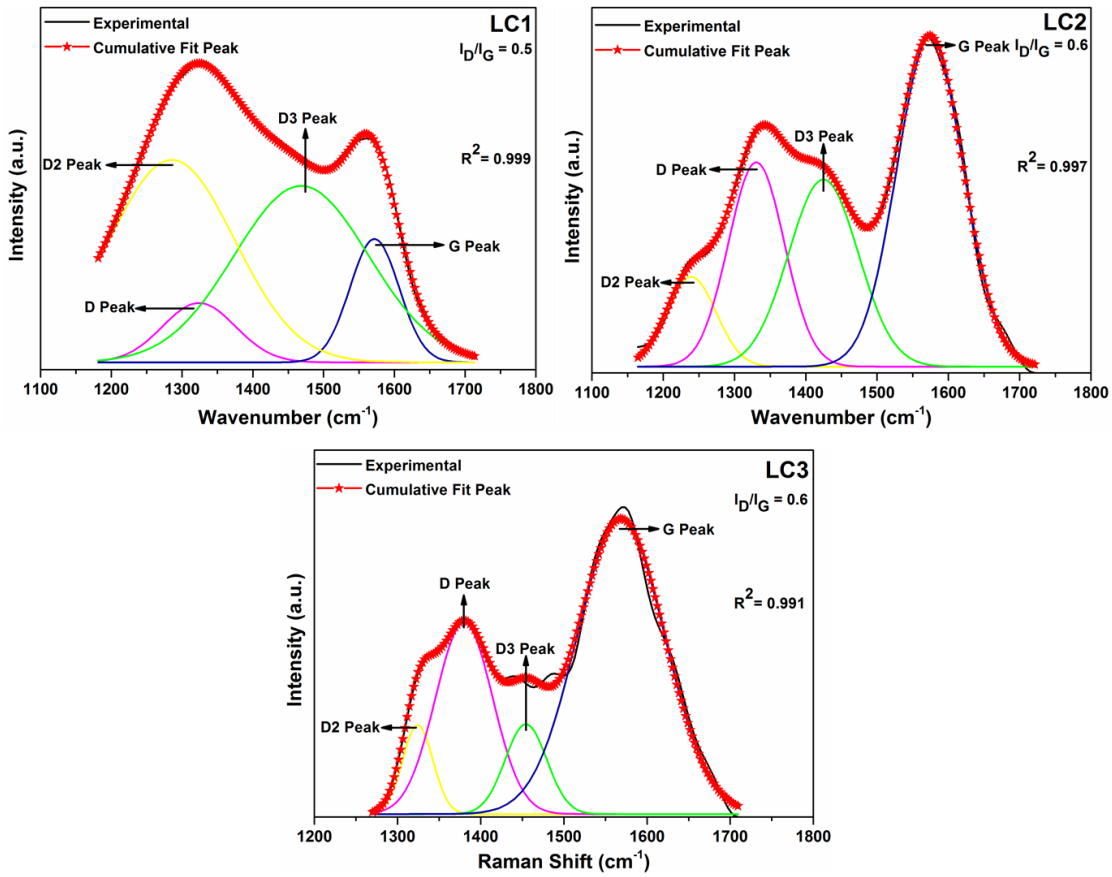

Figure 2: Deconvoluted first-order Raman spectra of lignite derived carbon nanostructures exhibiting peaks corresponding to different carbon species

Raman spectra of carbon nanostructures (LC1, LC2 & LC3) derived from low-grade coal lignite are presented in Figure 2. The broad Raman spectra in the range 1000-1815 cm^{-1} are deconvoluted to understand better the edge states and functional group defects in LC1, LC2, and LC3. Sadezky et al. (Sadezky, Muckenhuber, Grothe, Niessner, & Pöschl, 2005) described a five-peak model for fitting the Raman spectra of

carbon soot and related carbonaceous materials, and Sergi et al. (Claramunt et al., 2015) proposed a five-peak model for the fitting of Raman data of GO. Similarly, Rebelo et al. (Rebelo et al., 2016) recently proposed a multi-peak Raman fitting for the multiwalled CNTs and studied the covalent functionalization by diazonium chemistry and oxidation methodologies. In the present case, we find that four peaks were necessary to fit the broad Raman spectra of carbon nanostructures. Raman analysis of the as-synthesized carbon nanostructures (Figure 2) revealed the existence of defect (D) band (at ~1324 cm^{-1}, ~1331 cm^{-1}, ~1380 cm^{-1} for LC1, LC2 and LC3 respectively), graphitic (G) band (at ~1572 cm^{-1}, ~1574 cm^{-1}, ~1568 cm^{-1} for LC1, LC2 and LC3 respectively), D2 band (at ~1286 cm^{-1}, ~1239 cm^{-1}, ~1324 cm^{-1} for LC1, LC2 and LC3 respectively), and D3 band (at ~1468 cm^{-1}, ~1425 cm^{-1}, ~1454 cm^{-1} for LC1, LC2 and LC3 respectively). In addition to the well-known D and G Raman modes, the experimental data are fitted with novel Raman modes D2 and D3. Structural defects generated during the cutting (growth) or attachment of different functional groups in carbon nanostructures cause some Raman-inactive modes to become active. The edge is a kind of disorder, and the intensity of the Raman D band may be used to investigate the nature of edges. The momentum conservation law creates the D band due to the formation of edge states (zig-zag and armchair). The G band is produced by the in-plane vibrations of sp^2 carbon (E_{2g} mode). Additional bands, D2 and D3, may be associated with functional group defects. The D2 band may be attributed to COOH/C-OH functional groups and the D3 band due to the covalent bond formation between the oxygen and the edge carbon atoms, i.e., C=O/C-O bonds. The defect (ID) to graphitic (IG) band intensity ratio is 0.5, 0.6, and 0.6 for LC1, LC2, and LC3, respectively, indicating the formation of defects in the carbon nanostructures and the dialysis separation does not cause a difference in the density of defects.

4.1.2. Morphological analysis of the as-synthesized carbon nanostructures

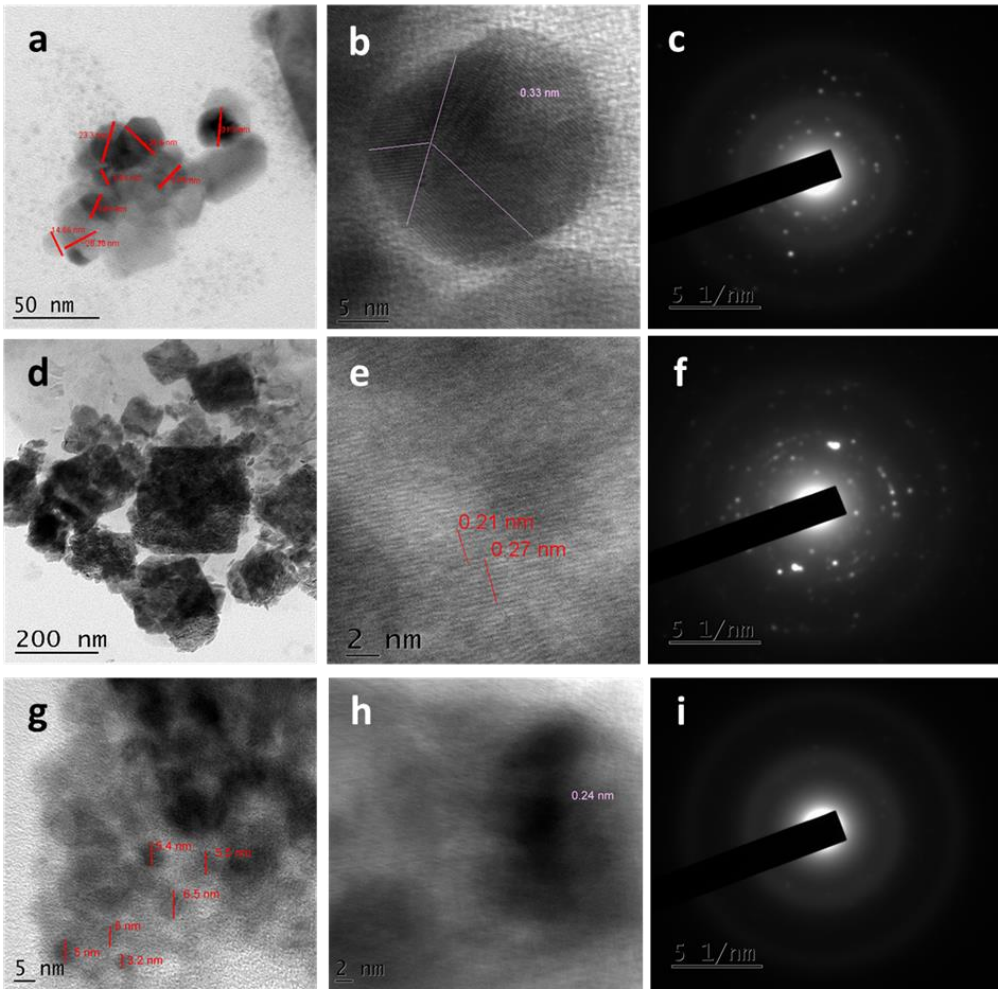

Figure 3: HRTEM images of the lignite derived carbon nanostructures with their SAED pattern. (a, b) LC1 portraying agglomerated graphene quantum dots with nano-crystallinity, (d, e) LC2 revealing agglomerated bulky nano-crystalline graphene quantum dots and (g, h) LC3 portraying agglomerated graphene quantum dots with lesser nano-crystallinity. c, f and i are SAED patterns of LC1, LC2 and LC3 respectively.

The morphology of the nanostructures is further analysed by a high-resolution transmission electron microscope (HRTEM) and is presented in Figure 3(a–i). One could observe the formation of heterogeneous graphene quantum dots (GQDs) of the shapes, hexagonal, pentagonal, and spherical nanoparticles in the residue (LC1) with the lateral size of the order of 10–23 nm (Figure 3a). The lattice fringe is measured to be ~0.31 nm confirming the presence of crystalline planes of graphene (Figure 3b) (Xiao, Liu, & Yang, 2015). The selected area electron diffraction (SAED) pattern of LC1 shows the nanocrystalline nature of nanocarbon (Figure 3c).

The HRTEM analysis of the synthesized nanostructure LC2 obtained after dialysis using the membrane filter and LC3 are presented in Figure 3(d-i). The sample inside the dialysis membrane (LC2) is stacked to form agglomerated bulky nano-crystalline graphene quantum dots (Figure 3d) whereas one could see an extensive collection of spherical nanoparticles with smaller size of the order of ~5 nm in the HRTEM images of permeate (LC3) (Figure 3g). The lattice fringe of LC2 is measured to be ~0.21 nm and ~0.27 nm (Figure 3e) whereas the lattice fringe of the permeate (LC3) is measured to be ~0.24 nm (Figure 3h). The LC3 GQDs are homogeneous and have a uniform size with a tendency to agglomerate (Figure 3g). The SAED pattern of LC2 show rings, which can be attributed to the nanocrystalline nature (Figure 3f) whereas the SAED pattern of permeate (LC3) shows an amorphous and slight nanocrystalline nature (Figure 3i) (Baker & Baker, 2010).

4.1.3. Optical behaviour of the as-synthesized carbon nanostructures

The lignite derived carbon nanostructures display substantial optical absorption in the ultraviolet range (Figure 4(a-c)), with a long tail extending into the visible area. All three carbon nanostructures show strong absorbance in the range of deep UV (<250 nm), which can be ascribed to π-π* transition of C=C bonds (Shang et al., 2012). The absorbance of LC1 and LC3 (permeate) had a small shoulder around 280 nm, while LC2 (sample inside the dialysis membrane) showed much stronger absorbance extended up to 450 nm, indicating mid-gap states in LC2. This absorbance band is consistent with n- π* transition of C=O or COOH groups (Ding et al., 2020; Yang et al., 2020).

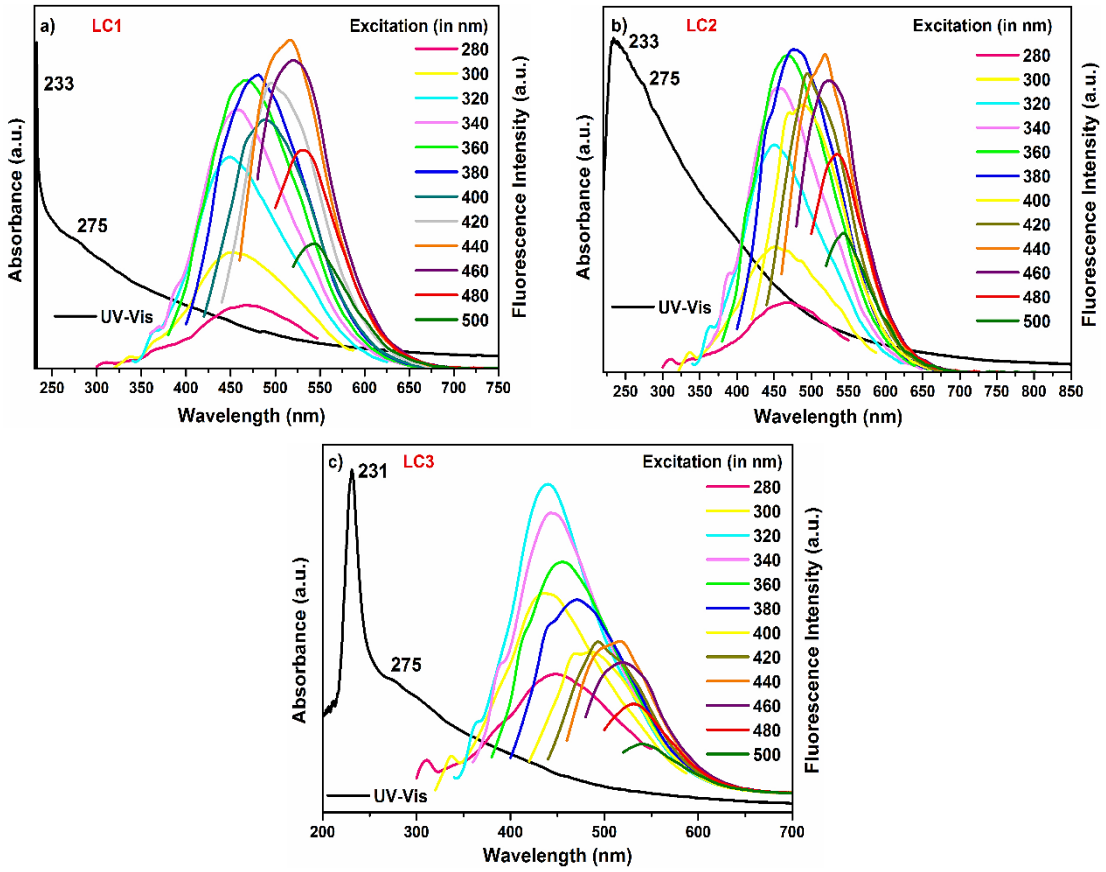

Figure 4: UV-Visible and fluorescence emission spectra of the lignite derived carbon nanostructures (a) LC1, b) LC2, and c) LC3)

The fluorescence spectra of the carbon nanostructures are recorded by varying the excitation wavelength from 280 to 500 nm with an interval of 20 nm (Figure 4). Fluorescence excitation spectra of LC1, LC2 and LC3 are consistent with the features of absorption showing pronounced excitation bands at 369 nm, 412 nm and 360 nm spectra respectively. The fluorescence emission spectrum of lignite derived carbon nanostructures shows excitation-dependent: a) blue emission and b) green emission where LC1 and LC3 (permeate) exhibit maximum fluorescence emission in the blue region and LC2 (sample inside the dialysis membrane) exhibit maximum fluorescence emission in the green region. Blue fluorescence was observed when the excitation wavelength was varied from 280 nm to 420 nm, followed by green fluorescence for excitation wavelengths 440 nm to 500 nm.

Each functional group in carbon nanostructures has optimal excitation and emission bands. In particular, the O-H groups are prominent at first, and the greatest emission is blue when excited by UV light. Simultaneously, this excitation wavelength

can also produce green and yellow emission, but their fluorescence intensity is lesser than that of blue emission. Then when excited by the blue light, the C=O functional groups dominate, resulting in the strongest emission shift to green colour. Therefore, the fluorescence of carbon nanostructures is attributed to the cooperation and competition between OH and COOH functional groups (Xiao, Liu, Li, et al., 2015).

The cooperation is reflected in the variation of the colour of fluorescence from blue to green when excited at various energies. The competition is expressed in the shift of the optimum excitation and emission wavelengths, that is, the position of the strongest emission peak. Due to the fact that each functional group has optimum excitation and emission wavelengths, when the excitation wavelength is changed, the corresponding emission wavelength varies correspondingly, resulting in an excitation-dependent fluorescence. FTIR spectrum analysis also confirms the dominance of hydroxyl and carbonyl functional groups in the lignite derived carbon nanostructures. The fluorescence spectrum ranges from 380 nm to 700 nm, with an fwhm of ~110–170 nm, which concludes that it can excite multiple bands at the same time.

The luminescence decay profiles of the three synthesized products (LC1, LC2, and LC3) are recorded at room temperature by a time-correlated single-photon counting technique. The fluorescence lifetime of the samples was fitted with a triple exponential function containing one fast component and two slow components (Figure 5a). The observed lifetime of LC1, LC2, and LC3 are ~5.3 ns, ~3.6 ns, and ~5.5 ns, respectively as depicted in Figure 5b.

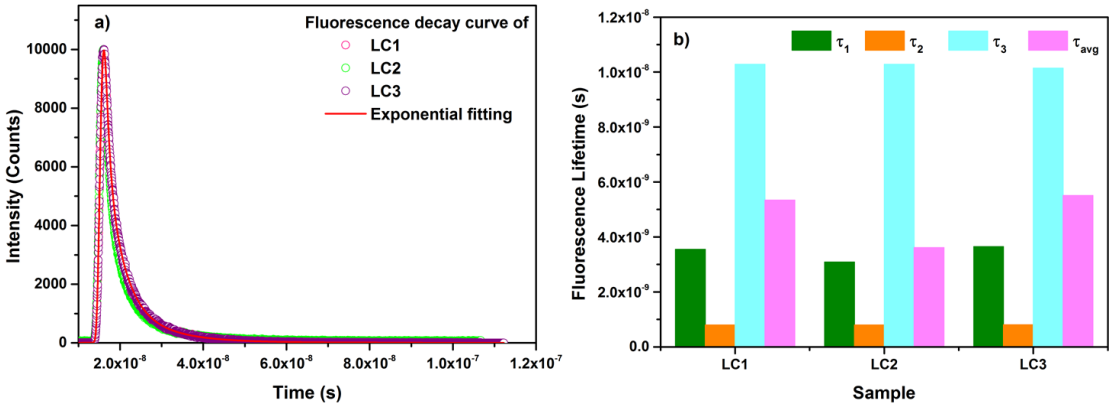

Figure 5: (a) Fluorescence lifetime decay curve of the lignite derived carbon nanostructures, (b) Fluorescence lifetime components of the lignite derived carbon nanostructures

Effect of solvent pH on fluorescence property of the synthesized nanoparticle was investigated at different pH (Acidic-4, Neutral-7, and Basic-9) and it is observed

that the position of fluorescence spectra of all the three samples is pH independent. But the fluorescence intensity was comparatively less in acidic pH.

To further evaluate the optical performance of the carbon nanostructures, fluorescence quantum yield was measured against standard quinine sulphate and determined to be around 0.2 - 1.08 %. The fluorescence emission profile of the carbon nanostructures was examined after exposure to illumination for 5 h, and only a minimal observable photo-bleaching was witnessed (<4%), authenticating the excellent photo-stability of the synthesized nanomaterials. The high fluorescence quantum yield, the long fluorescence lifetime, and the remarkable photo-stability of the as-synthesized carbon nanostructures make them promising materials for multidisciplinary applications.

The morphological, optical, structural, and compositional analyses of the lignite derived carbon nanostructures reveal the successful conversion of low-grade coal to value-added fluorescent carbon nanostructures. The samples exhibit outstanding optical properties like long fluorescence lifetime, and remarkable fluorescence stability along with tailorable surface chemistry, making them ideal candidates for fluorescence sensing applications.

4.1.4. Analytical application of the as-synthesized carbon nanostructures

The lignite-derived carbon nanostructures have high fluorescent stability and remarkable fluorescence properties; one promising application is a probe for metal ion detection in checking water contamination and biosensing. The change in fluorescence emission of the carbon nanostructures in buffer in the presence of various metal ions are investigated. The metal ions tested include potassium (K^+), calcium (Ca^{2+}), magnesium (Mg^{2+}), ferrous (Fe^{3+}), chromium (Cr^{2+}), nickel (Ni^{2+}), zinc (Zn^{2+}), lead (Pb^{2+}), sodium (Na^+), manganese (Mn^{2+}) and copper (Cu^{2+}). Notably, out of the eleven metal ions tested LC1, LC2 and LC3 shows high selectivity towards Cu^{2+} ions by fluorescence quenching (Figure 6). In comparison to LC1 and LC2, LC3 sample detect Cu^{2+} ions to a low concentration of 125 ppb at neutral pH and was investigated further to a picomolar concentration range.

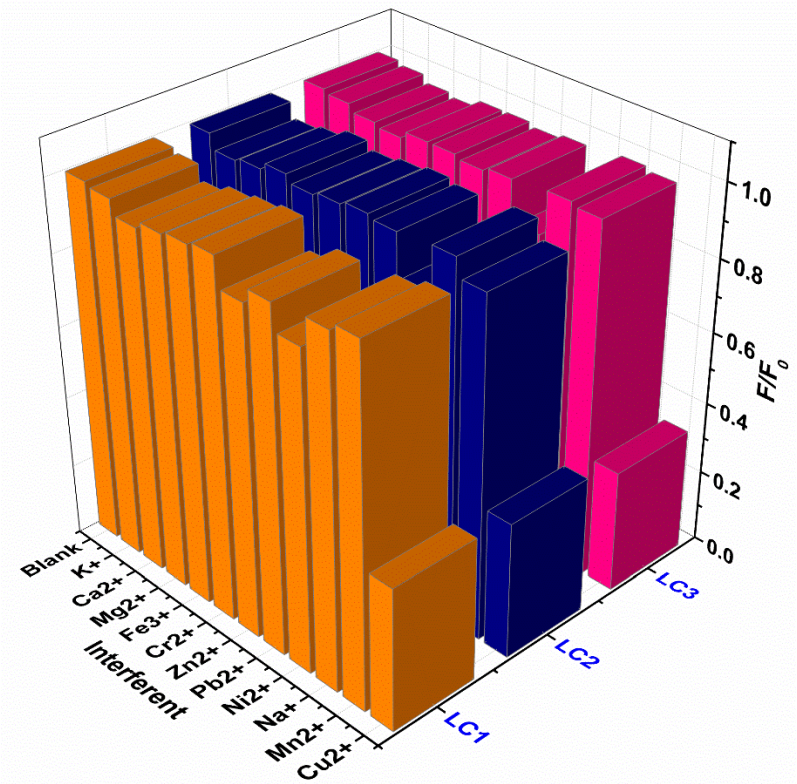

Figure 6: Selectivity of lignite-derived carbon nanostructures as probe for metal ions sensing in PBS buffer (pH 7, the concentration of each metal ion is 30 ppm; the content of nanoparticles is 25 µg/mL).

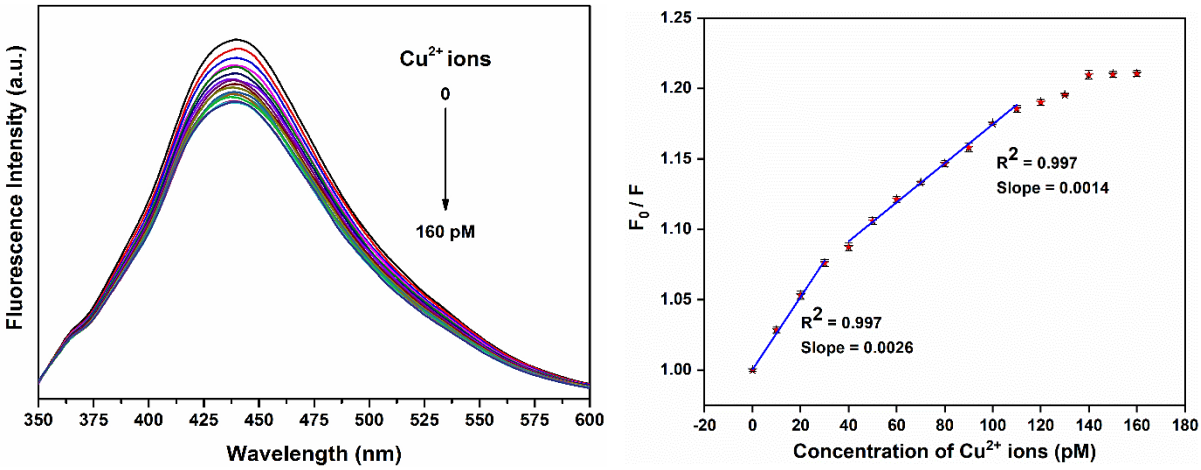

Figure 7: (a) Fluorescence emission spectra of carbon nanostructures (λ_{ex} = 320 nm) for increasing concentrations of Cu^{2+} ions in PBS (pH = 7). (b) The relative intensity (F_0/F) plot of fluorescence quenching of carbon nanostructures for varying concentrations of Cu^{2+} ions (Stern Volmer Plot), exhibiting linear range (F_0 and F, represent the fluorescence intensity of carbon nanostructures in the absence and presence of Cu^{2+} ions).

In the absence of Cu^{2+} ions, LC3 displayed a strong fluorescence emission spectrum centered at 438 nm (λ_{ex} = 320 nm), whereas, upon the gradual addition of successive aliquots of Cu^{2+} ions, LC3 experienced fluorescence quenching. Figure 7b displays the Stern-Volmer plot for fluorescence quenching of LC3 by Cu^{2+} ions, exhibiting a dual linear relationship in the concentration ranges from 10 pM to 30 pM and 30 pM to 110 pM. The regression equations of the relation are given by: $y_1 = 1.001 + 0.0025$ C (pM) and $y_2 = 1.035 + 0.0014$ C (pM), and the coefficients of determination are computed to be $R^2 = 0.996$ and $R^2 = 0.997$, fitted from the least-squares method. The limits of detection (LOD) of the equations are estimated to be as low as 1.32 pM and 2.35 pM, and the limits of quantification (LOQ) of the equations are estimated to be 4 pM and 7.14 pM. The fluorescence quenching can be ascribed to the electron transfer from the excited state of LC3 to Cu^{2+} as described in the Figure 8. Since Cu^{2+} could form a metal complex through the strong electrostatic attraction and rapid chelation with the amino groups on the surface of LC3, Cu^{2+} as an electron acceptor could facilitate the photo-induced electron transfer from LC3. This could be the reason for selectively detecting Cu^{2+}(Tam et al. 2018).

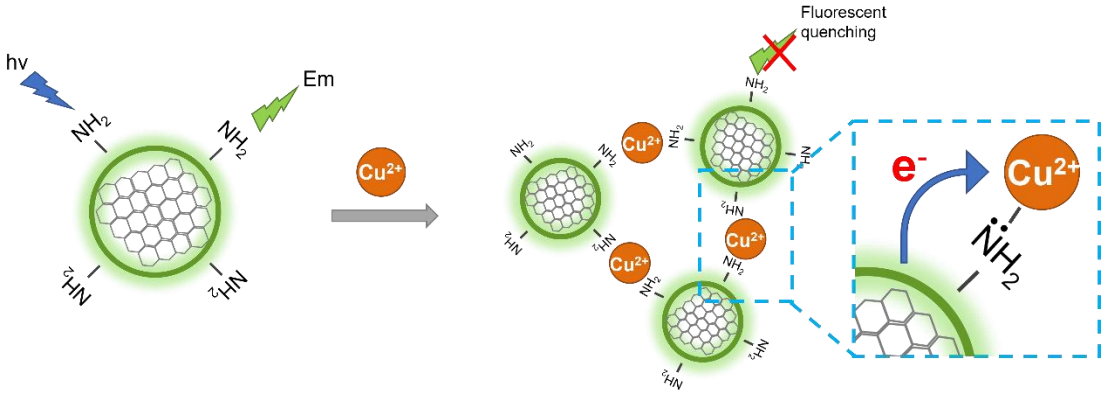

Figure 8: Schematic presentation of the fluorescence quenching mechanism of LC3 in the presence of Cu^{2+}

To ensure the applicability of LC3 sensor in real-life detection, copper ions spiked in water samples (lake water and tap water) using the standard addition method were detected. Briefly, three different copper ion concentrations were spiked in lake water and tap water. The fluorescence spectra were recorded at an excitation wavelength of 320 nm, and emission intensity was monitored at 438 nm wavelength. From the data collected from triplicate experiments, the concentrations of spiked samples were calculated from the plots and the values are tabulated in Table 1. The

recovery rates of copper ions ranged from 98.18% to 101.2%, with Relative Standard Deviations (RSDs) of less than 0.4%, indicating the accuracy of the fabricated sensor.

Table 1: Analytical performance of the as-prepared carbon nanostructures sensor for various concentrations of copper ions in lake water and tap water

Sensor	Formulation	Copper ions			
		Spiked (pM)	Found (pM)	RSD (%)	Recovery (%)
LC3	Lake Water	10	9.97	0.40	99.69
		20	20.24	0.36	101.2
		30	29.53	0.38	98.43
	Tap Water	10	9.95	0.36	99.53
		20	19.64	0.38	98.18
		30	29.60	0.40	98.68

4.1.5. Conclusion

In this study, carbon nanostructures were synthesized by a simple, scalable, and economical technique and the as-prepared carbon nanostructures, namely LC1, LC2 and LC3, demonstrated excellent fluorescence characteristics. LC3 exhibited remarkable copper ion sensing with a dual linear range with limits of detection (LOD) as low as 1.32 pM and 2.35 pM, and limits of quantification (LOQ) 4 pM and 7.14 pM. The recovery rates of copper ions ranged from 98.18% to 101.2%, with Relative Standard Deviations (RSDs) of less than 0.4%, indicating the accuracy of the fabricated sensor. The results are captivating, implying that these lignite derived carbon nanostructures could be employed to efficiently and economically detect low concentrations of copper ions in water.

The study pertaining to this is being published in the journal ‘Scientific Reports’ (impact factor - 4.379) titled as “Tunable direct band gap photoluminescent organic semiconducting nanoparticles from lignite”.

4.2. LIGNITE DERIVED FLUORESCENT CARBON NANOSTRUCTURES FOR NONINVASIVE MICROMOLAR GLUCOSE DETECTION

In the current study, carbon nanostructures (LR100, LR150, and LR200) are synthesized from low-grade coal lignite and the role of synthesis temperature on the

structure, composition, morphology, and optical characterizations are explored and as-synthesized carbon nanostructures are utilized for the fluorescence sensing of glucose.

4.2.1. Structure and composition of the as-synthesized nanocarbon

In this study, carbon nanostructures of different structure, composition, morphology and optical characterizations are synthesized by varying the synthesis temperature from low-grade coal lignite and the as-synthesized carbon nanostructures are utilized for the fluorescence sensing of glucose.

The X-ray diffraction pattern of the as-synthesized carbon nanostructures is shown in Figure 9. The broad peak observed at 23.6° corresponds to the reflection from 002 planes of graphitic carbon (Dong et al., 2014).

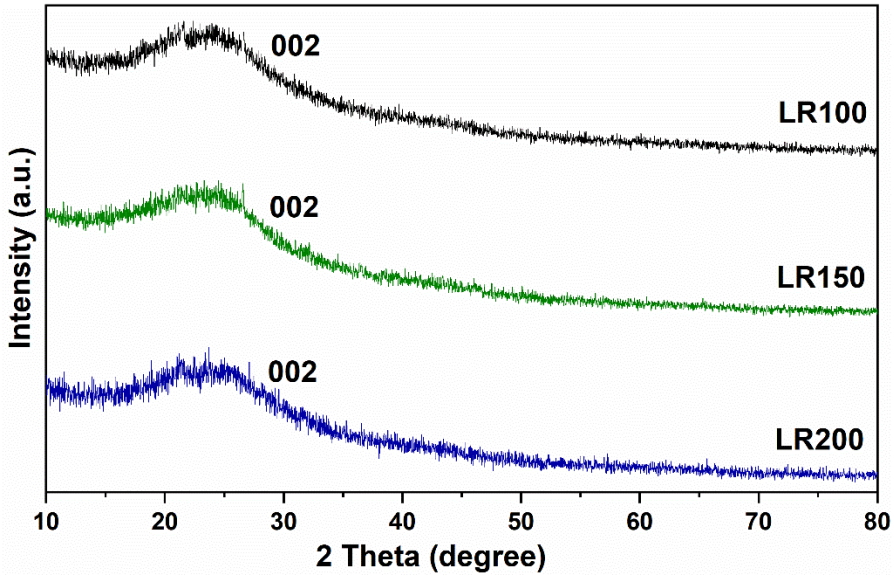

Figure 9: XRD spectra of as-synthesized carbon nanostructures exhibiting the presence of 002 planes of graphitic carbon

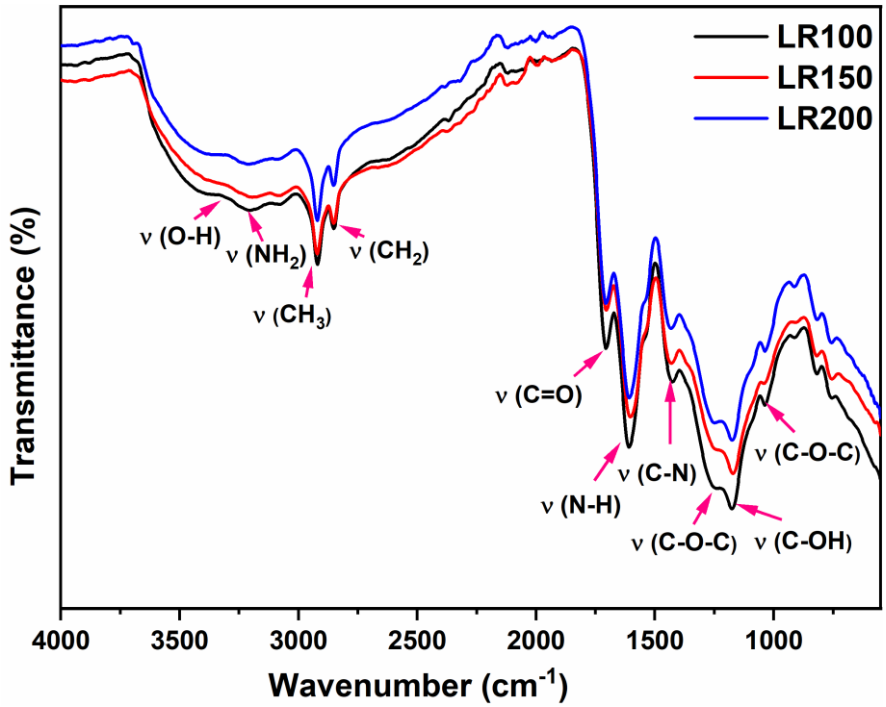

Figure 10: FTIR Spectra of as-synthesized carbon nanostructures exhibiting the presence of oxygen functional groups

The FTIR spectra of carbon nanostructures synthesized at 100°C, 150°C and 200°C are presented in Figure 10. The spectra have prominent peaks at 3500–3200 cm^{-}1, 2920 cm^{-1}, 2851 cm^{-1}, 1705 cm^{-1}, 1610 cm^{-1}, 1430 cm^{-1}, 1255 cm^{-1}, 1175 cm^{-1} and 1035 cm^{-1} and the descriptions for peak assignments are provided in Table 2 (Balachandran, 2014). As the synthesis temperature increased, FTIR spectra of carbon nanostructures revealed a decrease in the stretching of O–H and NH_2 (3200–3500 cm^{-1}, 1175 cm^{-1}), CH_3 group (2920 cm^{-1}), and CH_2 group (2851 cm^{-1}), which can be attributed to the acceleration of dehydration reaction which resulted in a decrease in the polar functional groups with an increase in synthesis temperature. The – C-N stretching (1351 cm^{-1}) and C-O (epoxy) (1255, 1035) stretching decreased with the increasing synthesis temperature. Intensities of N-H stretching (1633 cm^{-1}) and C=O (carbonyl/carboxyl) stretching (1705) also decreased with temperature which may suggest amino compounds and carbonyl/carboxyl compounds has been degraded. The maximum loss was obtained in –OH, –CH_2, and C–O functional groups as a function of synthesis temperature.

Table 2. Functional groups observed in the Fourier-transform infrared (FTIR) spectra of lignite derived carbon nanostructures produced at different temperatures.

Wave Numbers (cm^{-1})	**Characteristic Vibrations (Functionality)**

3500–3200	O–H and NH_2 stretching
2920	- CH_3 stretching
2851	- CH_2 stretching
1705	C=O (carbonyl/carboxyl) stretching
1633	- N-H stretching
1351	- C-N stretching
1255, 1035	C-O (epoxy) stretching
1175	O–H stretching

The Raman spectra of LR100, LR150, and LR200 are depicted in Figure 11.

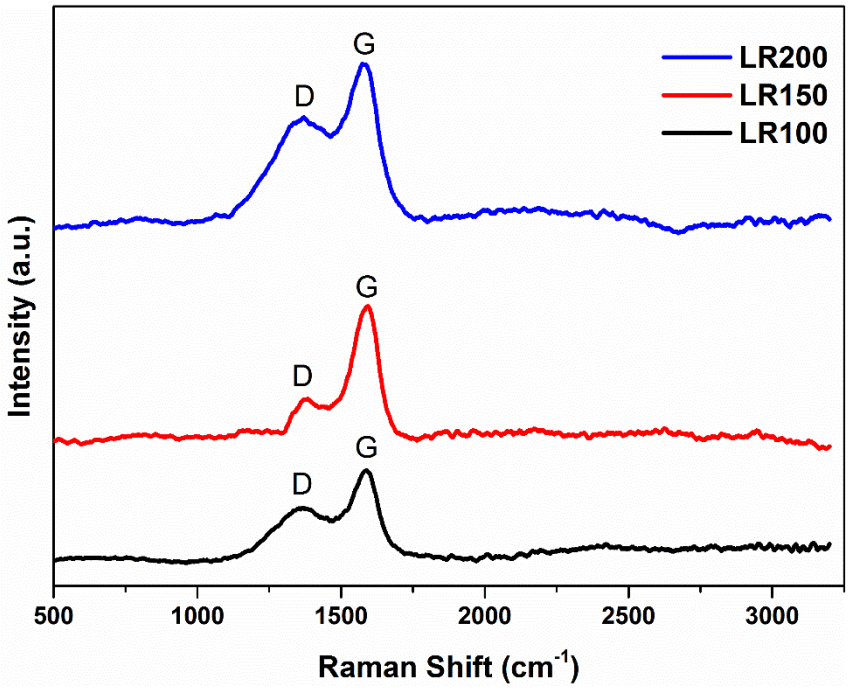

Figure 11: Raman spectra of as-synthesized carbon nanostructures exhibiting the D band and G band

The G band is produced by the in-plane vibrations of sp^2 carbon (E_{2g} mode), The D band is created by the momentum conservation law due to the formation of edge states (zig-zag and armchair) (Rao et al., 2009). The intensity of the Raman D band is very sensitive to the type of edge states. It is prominent on the armchair edges but almost non-existent on the zig-zag edge. The increase in synthesis temperature from 100°C to 150°C resulted in a G peak shift to higher frequency (1587 cm^{-1} to 1592 cm^{-1}) and then back to lower frequency (1580 cm^{-1}) when the synthesis temperature increased from 150°C to 200°C. Similarly D peak also showed a shift to higher frequency (1364 cm^{-1} to 1383 cm^{-1}) when the synthesis temperature increased from 100°C to 150°C followed

by a shift to lower frequency (1369 cm^{-1}) when the synthesis temperature increased from 150°C to 200°C. The I_D/I_G ratios of LR100, LR150, and LR200 are 0.58, 0.31, and 0.66 respectively which indicates a decrease in defective nature when the synthesis temperature increased from 100°C to 150°C followed by an increase in defective nature when the synthesis temperature increased from 150°C to 200°C which indicates that the increase in temperature has increased the density of edge-plane-like defective sites (Zhao et al., 2017).

4.2.2. Morphological analysis of the lignite derived carbon nanostructures

The surface morphology of the as-synthesized carbon nanostructures synthesized at a) 100°C, b) 150°C, and c) 200°C is depicted in Figure 12.

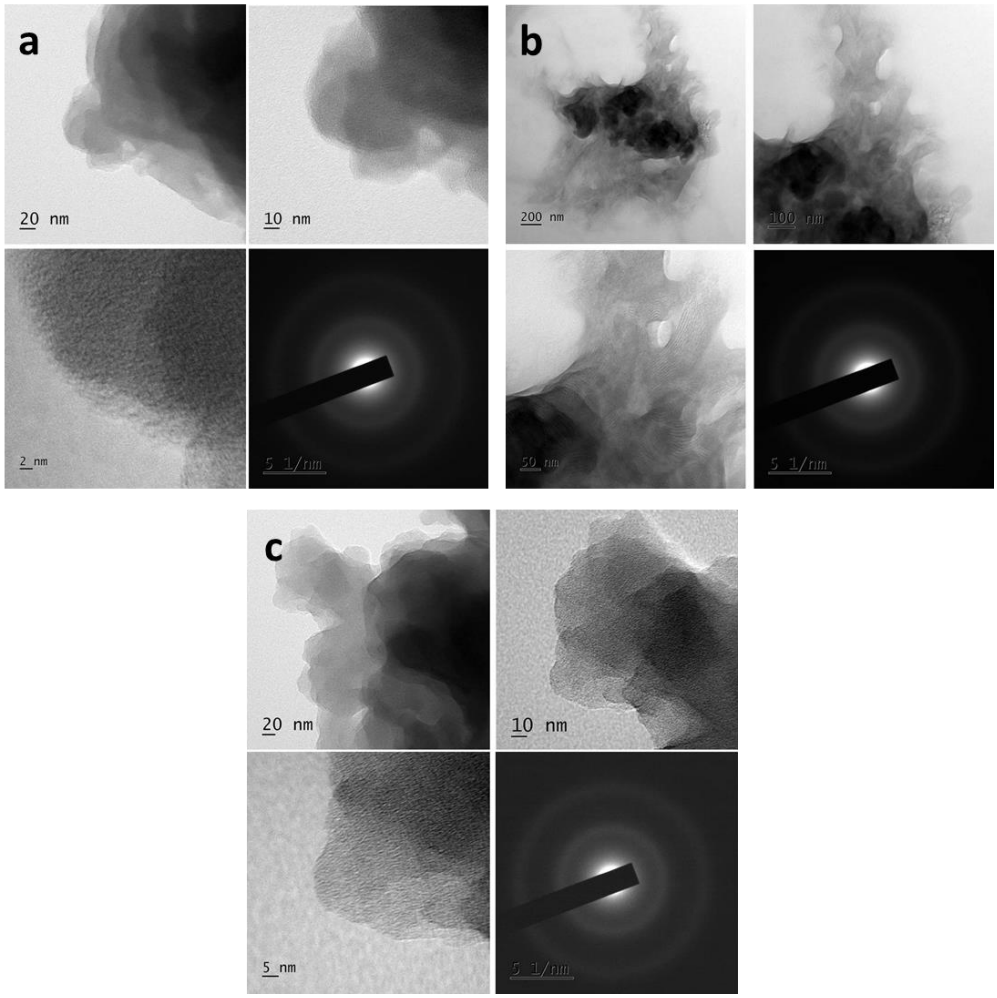

Figure 12: HRTEM images of the as-synthesized carbon nanostructures after thermal treatment (a) LR100, b) LR150 & c) LR200

The surface analysis confirms the formation of carbon nanostructures with different morphology produced at various synthesis temperatures. In the LR100 and LR200 samples, one can observe few-layered carbon nanosheets-like morphology,

while in the LR150 sample; a carbon nanoribbons structure is developed. Furthermore, the selected area electron diffraction (SAED) pattern demonstrates the amorphous nature of the nanostructures produced (Xiao, Liu, & Yang, 2015).

4.2.3. Optical behaviour of the lignite derived carbon nanostructures

The optical properties of LR100, LR150, and LR200 were studied in detail with the aid of UV Visible absorption spectra and fluorescence spectra.

The lignite derived carbon nanostructures display substantial optical absorption in the ultraviolet range (Figure 13), with a long tail extending into the visible area. The absorption peaks detected at around 270-280 nm and 300 nm in all the samples are caused by the characteristic π-π* transition of the C=C bond and n-π* transition of the C=O bond. The absorption peak at 279 nm shifted to shorter wavelength (267 nm) when the synthesis temperature increased from 100°C to 200°C indicating a decrease in the π –conjugation which means more energy is required for the transition. The absorption peak at 292 nm shifted to longer wavelength (303 nm) when the synthesis temperature increased from 100°C to 200°C. The optical bandgap of the samples synthesized at 100°C, 150°C and 200°C are calculated from the Tauc plot to be 3.9 eV, 3.9 eV, and 3.3 eV respectively (Zhao et al., 2017).

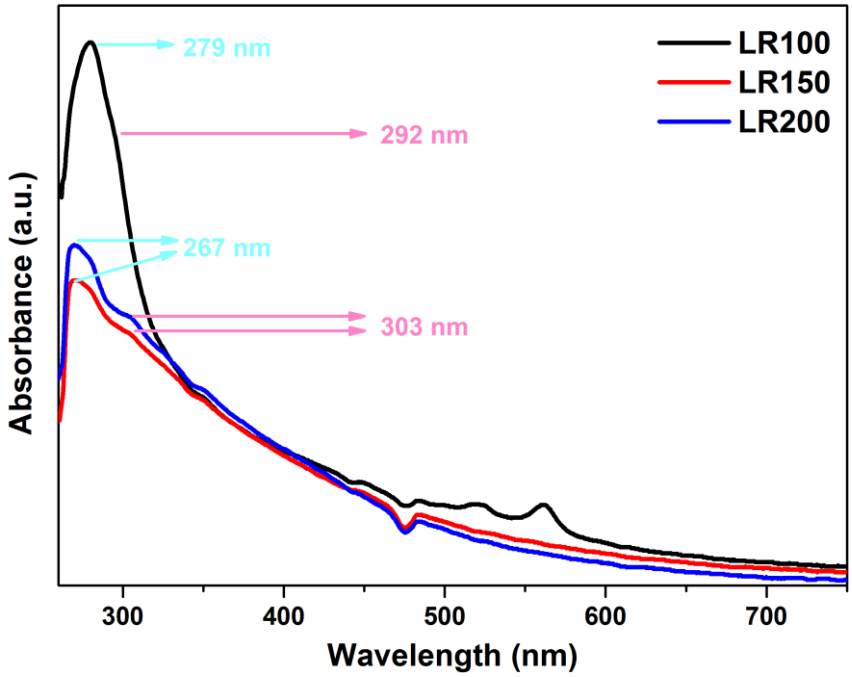

Figure 13: UV Visible spectra of as-synthesized carbon nanostructures exhibiting π-π* and n-π* transition

The fluorescence emission spectra of LR100, LR150, and LR200 were obtained at varying excitation wavelengths from 220 nm to 540 nm in steps of 10 nm (Figure 14).

The fluorescence spectrum of LR100 (Figure 14a) exhibits excitation independent emission spectra when excited with UV light and excitation dependent emission spectra when excited with visible light excitation. The excitation-independent fluorescence emission is centered on 450 nm (blue emission) at excitation wavelengths for the excitation ranging from 220 to 330 nm, with a decrease in fluorescence emission intensity when excited at 220 to 280 nm followed by an increase to 320 nm. From an excitation of 330 nm to 490 nm, the emission spectra show a redshift with a decrease in fluorescence intensity (excitation-dependent emission). The maximum fluorescence emission is observed at 449 nm at an excitation of 320 nm.

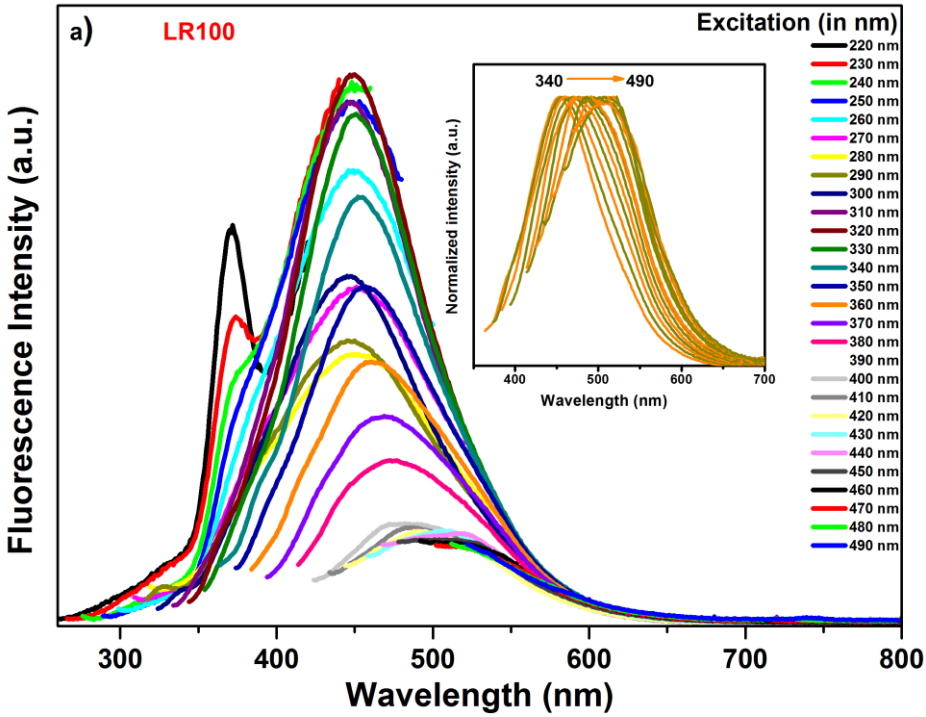

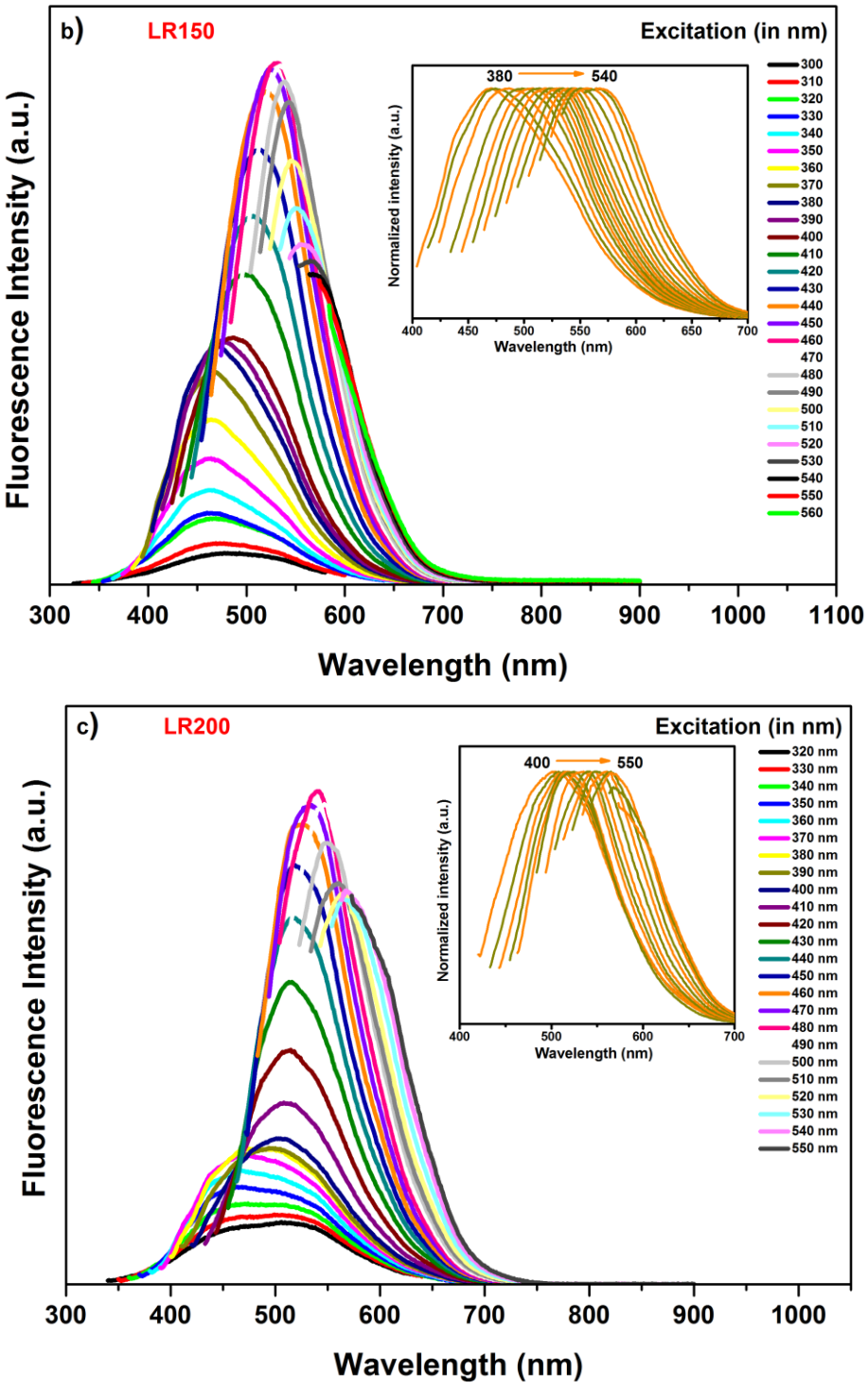

Figure 14: Fluorescence spectra of a) LR100, b) LR150, and c) LR200

The fluorescence spectrum of LR150 (Figure 14b) demonstrates excitation-independent fluorescence behaviour with an increase in fluorescence emission intensity when excited at a range of 320 nm to 370 nm. The emission spectra show a redshift (excitation dependent emission) upon excitation from 380 nm to 540 nm with an initial increase in intensity till an excitation wavelength of 480 nm followed by a

decrease. The maximum fluorescence emission is observed at 530 nm at an excitation of 460 nm.

When excited with UV light, the fluorescence spectrum of LR200 (Figure 14c) exhibits excitation independent emission, and when excited with visible light, it shows excitation-dependent emission behaviour. At excitation wavelengths varying from 320 to 380 nm, the excitation-independent fluorescence emission shows a rise in fluorescence emission intensity till 480 nm followed by a decline till 530 nm. Between 390 and 530 nm excitation, the emission spectra exhibit a redshift (excitation-dependent emission). The maximum fluorescence emission is observed at 539 nm at an excitation of 480 nm.

The luminescence decay profiles of the three synthesized products (LR100, LR150 and LR200) are recorded at room temperature by a time-correlated single-photon counting technique. The fluorescence lifetime of the samples was fitted with a triple exponential function containing one fast component and two slow components (Figure 15a). The observed lifetime of LR100, LR150 and LR200 are ~4.98 ns, ~4.87 ns, and ~4.28 ns, respectively as depicted in Figure 15b.

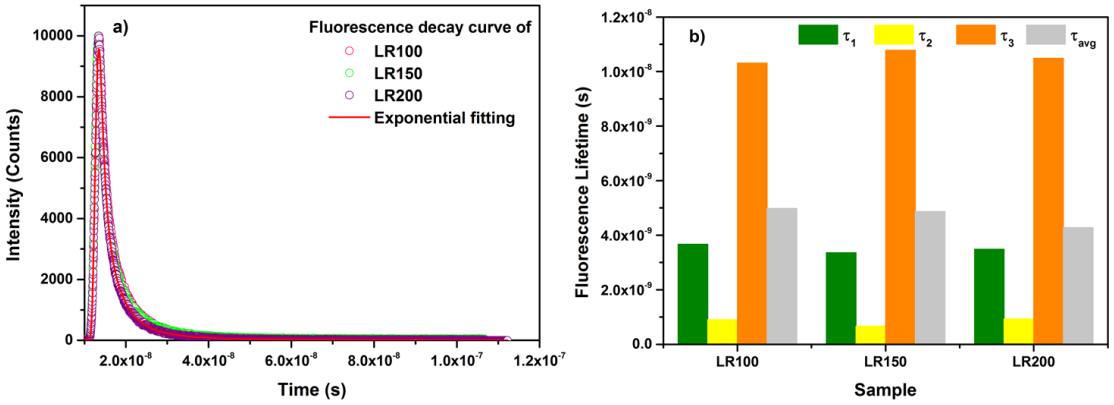

Figure 15: (a) Fluorescence lifetime decay curve of LR100, LR150 and LR200, (b) Fluorescence lifetime components of LR100, LR150 and LR200

Wang et al. (Yijie, Lei, & Haiyu, 2020), in their recent work, reported that the fast emission component (τ_1) is due to the oxygen functional groups, which might contribute to the fluorescence through electron transition n-σ* (for C-O-C and -OH) and n-π* (for C=O and –COOH). The τ_2 component is attributed to the π-π* transition of the aromatic core (sp^2 skeleton) of the carbon nanostructures. The τ_3 component is due to the disordered structure in the sample. The observed lifetime in nanoseconds suggests that the as-synthesized carbon nanostructures are suitable for imaging applications.

The excitation dependent fluorescence emission indicates that the photoluminescence of carbon nanostructures derived from coal comes from the surface state including the surface oxidation and surface functional groups. Mainly, the more surface defects there are, the more excitons (i.e., electrons and holes) can be trapped. Therefore, the radiation from the recombination of trapped excitons leads to the red-shifted emission. The different emissions (blue, green and red fluorescence) of carbon nanostructures are derived from varied transitions. The blue emission of carbon nanostructures arises from the radiative recombination of the excited electrons from the $n \rightarrow \pi^*$ transition of C=O. With the increase of O-containing groups (C-OH and C-O-C) on sp^2-hybridized carbons, numerous epoxide (or hydroxyl)-related localized electronic states form below π^* state, producing numerous new energy levels between $n \rightarrow \pi^*$ gaps. Therefore, the band gap reduces as oxygen content increases on the surface of carbon nanostructures, that is, fluorescence redshift result from the increase in the degree of surface oxidation (Liu, 2020).

To further evaluate the optical performance of the carbon nanostructures, fluorescence quantum yield was measured against standard quinine sulphate and determined to be around 1.2 %, 2.8 % and 12.5 % for LR100, LR150 and LR200. The fluorescence emission profile of the carbon nanostructures was examined after exposure to illumination for 5 h, and only a minimal observable photo-bleaching was witnessed (<4%), authenticating the excellent photo stability of the synthesized carbon nanostructures.

4.2.4. Efficacy of lignite derived nanocarbon as a glucose sensor

The efficiency of as-synthesized carbon nanostructures for glucose sensing was evaluated under optimum conditions with the aid of glucose oxidase (GOx). The change in the fluorescence intensity of LR100, LR150, and LR200 with varying glucose concentration (8-3000 µM) is shown in Figure 16(a, c and e) and Stern Volmer plot (Figure 15(b, d, and f)) is plotted in order to find the linear range of glucose detection and limit of detection. Stern Volmer plot obtained is in good agreement with the straight-line equation ($y = mx + c$), where x is the concentration of glucose molecule, y is F_0/F where F_0 and F are the fluorescence emission intensities observed in the absence and presence of analyte respectively, m is the slope and c is the intercept. The $(3*\sigma)/s$ formula is used to determine the limit of detection where σ is the standard deviation of the blank signal and s, the slope of the calibration plot (Wei et al., 2012). The limit of

quantitation was calculated using (10*σ)/s where σ is the standard deviation of the blank signal and s, the slope of the calibration plot (Yahyazadeh & Shemirani, 2019).

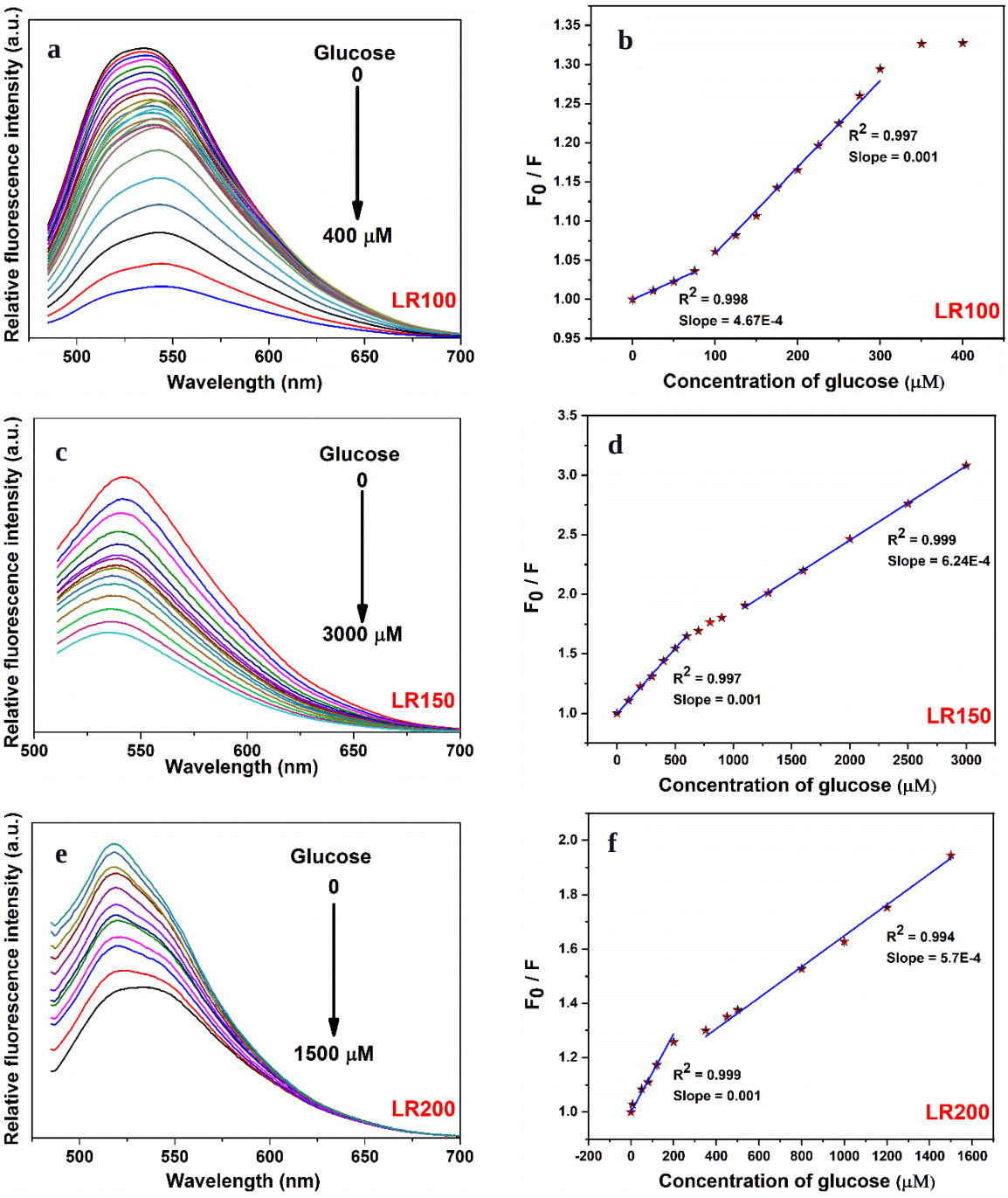

Figure 16: (a, c & e) Fluorescence emission spectra of LR100, LR150 and LR200 for increasing concentrations of glucose in DMF (pH- 6.3). (b, d & f) Stern-Volmer plots for fluorescence quenching of LR100, LR150 and LR200 for varying concentrations of glucose

Figure 16b displays the Stern-Volmer plot for fluorescence quenching of LR100 by glucose exhibiting a dual linear relationship in the concentration ranges from 25 μM to 75 μM and from 100 μM to 300 μM. The regression equations of the relation are given by: y1 = 0.99 + 4.67E-4 C (μM) and y2 = 0.95 + 0.001 C (μM) and the coefficients of determination are computed to be (R^2) 0.998 and 0.997 respectively, fitted from the least-squares method. The limit of detection (LOD) of the two regression equations is estimated to be as low as 7.07 μM and 3.3 μM, respectively. The limit of quantification (LOQ) of the two regression equations is estimated to be as low as 21.4 μM and 10 μM, respectively.

Figure 16d displays the Stern-Volmer plot for fluorescence quenching of LR150 by glucose exhibiting a unique dual linear relationship in the concentration ranges from 100 μM to 600 μM and from 1100 μM to 3000 μM. The regression equations of the relation are given by: y1 = 0.99 + 0.001 C (μM) and y2 = 1.21 + 6.24E-4 C (μM), and the coefficients of determination are computed to be (R^2) 0.997 and 0.999 respectively, fitted from the least-squares method. The limit of detection (LOD) of the two regression equations is estimated to be as low as 3.3 μM and 5.29 μM, respectively. The limit of quantification (LOQ) of the two regression equations is estimated to be as low as 10 μM and 16 μM, respectively.

Figure 16f displays the Stern-Volmer plot for fluorescence quenching of LR200 by glucose exhibiting a unique dual linear relationship in the concentration ranges from 8 μM to 120 μM and from 800 μM to 1500 μM. The regression equations of the relation are given by: y1 = 1.00 + 0.001 C (μM) and y2 = 1.08 + 5.71E-4 C (μM), and the coefficients of determination are computed to be (R^2) 0.999 and 0.994 respectively, fitted from the least-squares method. The limit of detection (LOD) of the two regression equations is estimated to be as low as 3.3 μM and 5.79 μM, respectively. The limit of quantification (LOQ) of the two regression equations is estimated to be as low as 10 μM and 17.5 μM, respectively.

Fluorescence measurements were performed in the presence of a fixed concentration (30 μM) of various interfering species, namely dopamine, uric acid, ascorbic acid, K^+, Ni^{2+}, Ca^{2+}, Mg^{2+}, Fe^{3+}, Na^+ and Mn^{2+} to assess the validity and test the selectivity of LR100, LR150, and LR200 sensors. Selectivity was evaluated by plotting the fluorescence intensity ratios of the sensors against the interfering species. As seen in Figure 17, glucose showed a remarkable quenching effect on the fluorescence emission intensities of the LR100, LR150, and LR200, whereas no

quenching/ negligible quenching was noticed in the presence of other interfering species. Furthermore, the relative error of the interference effect of common interferents was below 3%, which is within the tolerable limit. These observations confirm that the developed sensors are highly selective towards detecting glucose.

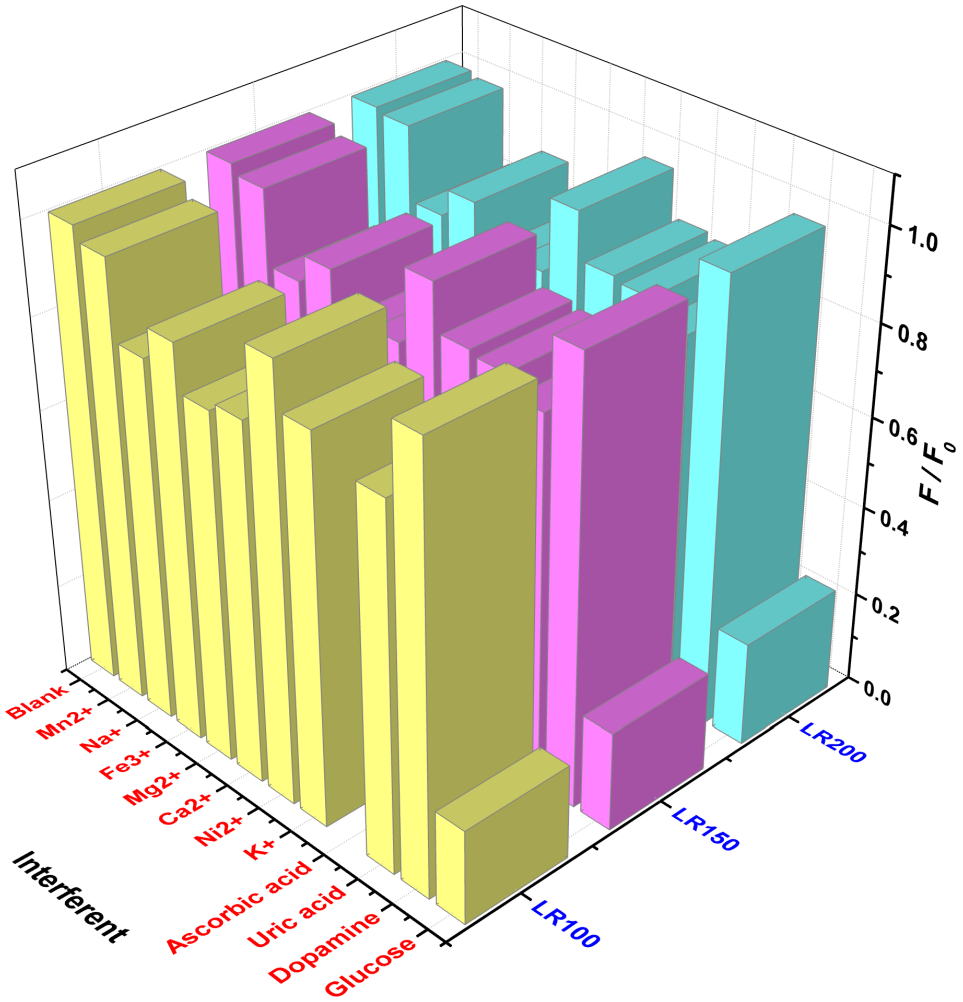

Figure 17: Fluorescence intensity ratio response of the LR100, LR150 and LR200 to Glucose and other potential interferents in PBS (interferents = 30 µM; LR100, LR150 & LR200 each = 25 µg/ml; solution pH = 7)

In an aqueous medium, the enzymatic oxidation of glucose generates d-gluconic acid and H_2O_2, with GOx acting as an oxidant. The following is the cyclic enzyme reaction:

$$\text{Glucose} + O_2 + H_2O \xrightarrow{\text{GOx}} \text{D-gluconic acid} + H_2O_2$$

Hydrogen peroxide is unstable. It decays according to the reaction:

$$2\ H_2O_2 \longrightarrow 2\ H_2O + O_2$$

The active oxygen species formed from the decaying of H_2O_2 interacts with the surface of the carbon nanostructures and captures the electrons at the conduction bands, inhibiting the photo induced electron and hole radiative recombination (Ghosh et al., 2018). As a result, the fluorescence intensity of the carbon nanostructures decreases. Furthermore, the O_2 generated by the redox reactions between H_2O_2 and as-synthesized carbon nanostructures may also catalyse the GOx reaction, giving in a cyclic electron transfer mechanism during glucose oxidation which is advantageous for the entire reaction mechanism (Figure 18).

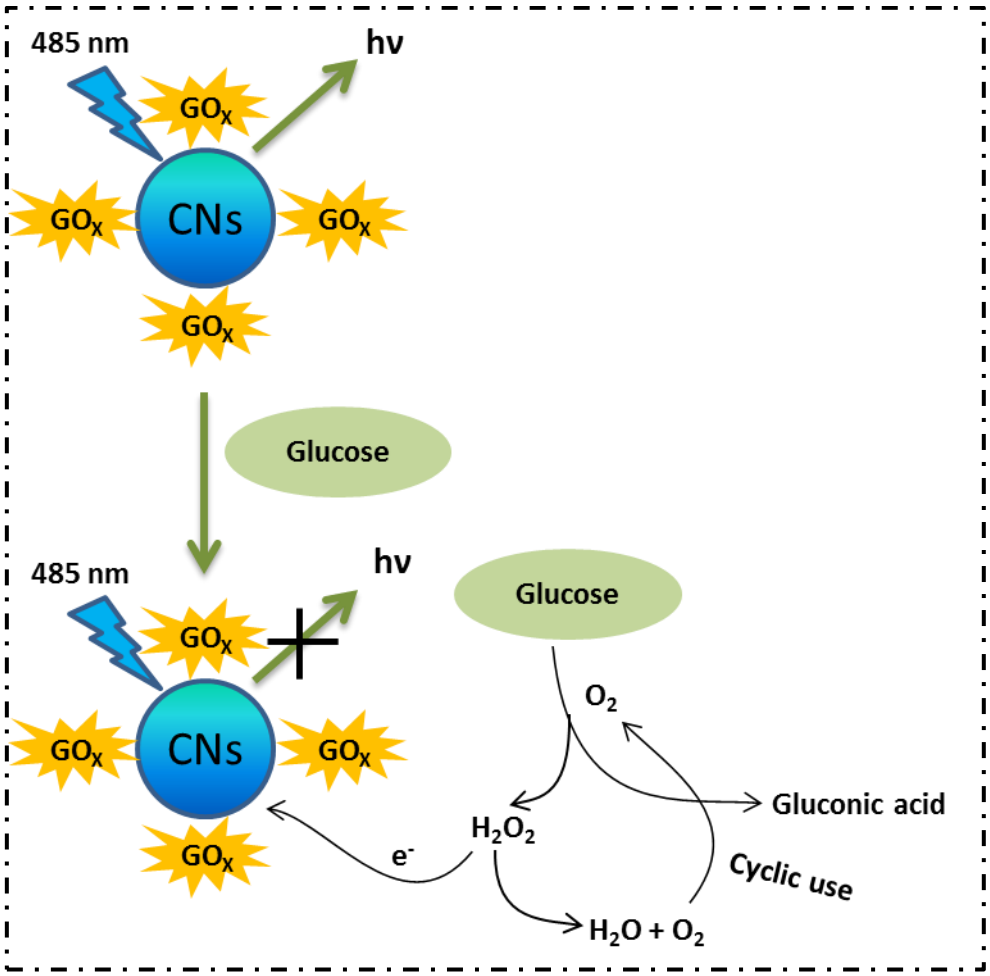

Figure 18: Illustration of glucose sensing mechanism by the lignite derived carbon nanostructures (CNs)

The quantitative detection of glucose with a high degree of sensitivity was accomplished using glucose oxidase based on the fluorescence of as-synthesized carbon nanostructures. The interaction of GOx and glucose is extremely specific. Wang et al. (G. Wang et al., 2014) demonstrated that various sugars such as fructose, sucrose, and lactose have a negligible effect on glucose detection, as GOx oxidizes glucose quite specifically. The enhancement of the sensing performance of as-synthesized carbon

nanostructures is dependent on optimizing various parameters of the enzymatic reaction, such as the GOx concentration, reaction duration, reaction temperature, and GOx immobilization method. Further modifications to the sensing properties of the studied system may be explored in future studies.

To ensure the applicability of LR100, LR150, and LR200 sensors in real-life detection, glucose spiked in biological samples (human urine and saliva) using the standard addition method were detected. Briefly, three different glucose concentrations were spiked in human urine and saliva. The fluorescence spectra were recorded at their respective fluorescence maxima excitation wavelength. From the data collected from triplicate experiments, the concentrations of spiked samples were calculated from the plots and the values are tabulated in Table 3. The recovery rates of glucose ranged from 98.19% to 102.17%, with Relative Standard Deviations (RSDs) of less than 0.4%, indicating the high accuracy of the fabricated sensor.

Table 3: Analytical performance of the as-prepared and the GCE modified LR100, LR150, and LR200 sensors for various concentrations of glucose in biological fluids

Sensor	**Formulation**	**Glucose**			
		Spiked (µM)	**Found (µM)**	**RSD (%)**	**Recovery (%)**
LR100	Human Urine	25	25.37	0.40	101.50
		50	50.45	0.38	100.90
		75	74.85	0.40	99.79
	Human Saliva	25	24.549	0.39	98.19
		50	50.9	0.39	101.8
		75	74.624	0.37	99.49
LR150	Human Urine	100	98.49	0.40	98.49
		200	201.20	0.40	100.60
		300	298.49	0.40	99.49
	Human Saliva	100	101.50	0.38	101.50
		200	197.59	0.37	98.79
		300	302.10	0.40	100.70
LR200	Human Urine	10	9.92	0.39	99.21
		20	19.83	0.38	99.16
		30	29.67	0.40	98.91
	Human Saliva	10	10.22	0.36	102.17
		20	20.25	0.38	101.28
		30	29.55	0.39	98.51

A comparison of the analytical parameters and the optical attributes of the as synthesized and the modified LR100, LR150, and LR200 sensors is shown in Table 4.

Table 4: A comparison of the analytical performance and optical behaviour of the as-prepared and the modified LR100, LR150, and LR200 sensors

	LR100	**LR150**	**LR200**
Detection Range (µM)	25-75 100-300	100-1000 1000-3000	8-120 800-1500
Limit of Detection (µM)	6.8 3.3	30 48.23	1.65 5.48
Limit of Quantification (µM)	20.9 10	100 160.7	5 16.6
Quenching Efficiency (%)	82.21	64.37	48.59
Quantum Yield (%)	1.2	2.8	12.5
Fluorescence Lifetime (ns)	4.98	4.87	4.28

Of all the sensors, LR200 exhibits better fluorescence quantum yield along with a lower limit of detection, best suited for precise quantification of the glucose in actual samples, with significant potential for use in diabetic management.

4.2.5. Conclusion

In this study, carbon nanostructures were synthesized from lignite using a simple, scalable, and economical technique at the synthesis temperatures 100°C, 150°C, and 200°C and the as-prepared carbon nanostructures, namely LR100, LR150, and LR200 demonstrated excellent fluorescence characteristics. All the three samples, exhibited remarkable glucose sensing with a dual linear range with limits of detection (LOD) as low as 3.3 µM and limits of quantification (LOQ) 10 µM by LR200. The recovery rates of glucose ranged from 98.19% to 102.17%, with Relative Standard Deviations (RSDs) of less than 0.4%, indicating the high accuracy of the fabricated

sensor. LR200 has the highest fluorescence quantum yield and the lowest detection limit of the three sensors, making it the most suitable for exact measurement of glucose in real samples, with substantial promise for application in diabetes care.

The study pertaining to this is being communicated in the journal "Analytica Chimica Acta" titled as "Low-grade coal-derived carbon nanostructures as a sensitive fluorescence probe for micromolar glucose detection".

4.3. LIGNITE DERIVED CARBON NANOSTRUCTURES FOR SIMULTANEOUS ELECTROCHEMICAL SENSING OF HEAVY METAL IONS CADMIUM AND LEAD

In this study, we firstly report a new application of low-grade lignite as unique modified electrode material in electrochemical sensing, producing good electrochemical performance similar with graphene and makes the utilization of lignite become more multi-purpose and more meaningful. One of the main steps during the synthesis of these carbon nanostructures is the annealing of lignite at 400°C which leads to lots of edge-plane-like defective sites and low charge transfer resistance, resulting in good electron transfer efficiency and excellent electro catalytic activity, making it a promising signal amplifier material and modified matrix in electrochemical sensing. Here, lignite derived carbon nanostructures are utilized for the simultaneous electrochemical sensing of heavy metal ions lead (Pb) and cadmium (Cd).

4.3.1. Structure and composition of the as-synthesized carbon nanostructures

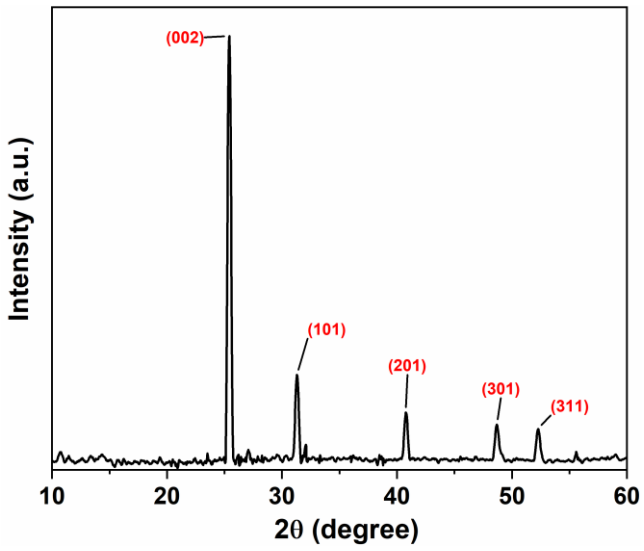

Figure 19: XRD spectrum of LA400 exhibiting the presence of (002), (101), (201), (301), and (311) planes of graphitic carbon

X-ray diffractogram of LA400 (Figure 19) exhibits a prominent peak at 25º corresponding to (002) plane of graphitic carbon and appearance of peaks at 31º, 41º, 48º and 52º corresponding to (101), (201), (301), and (311) planes of graphitic carbon.

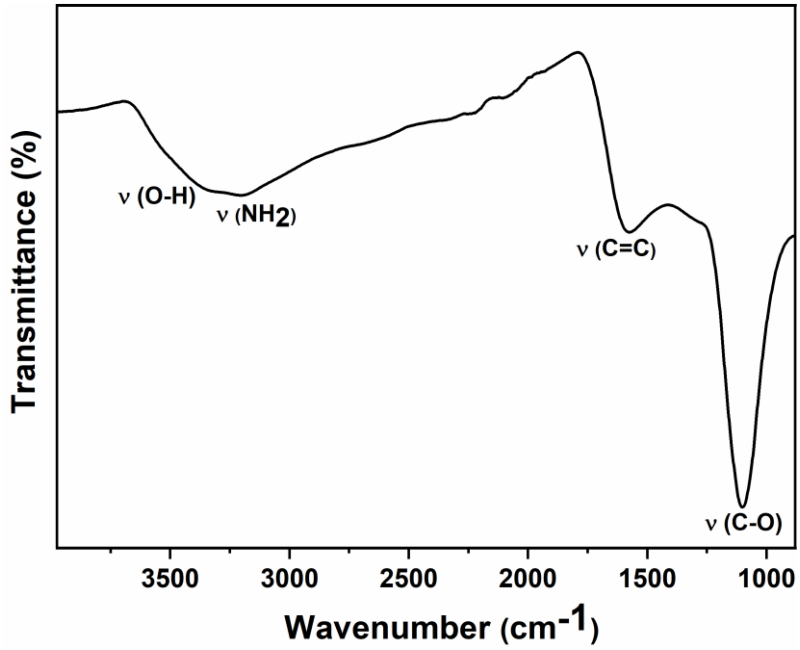

Figure 20: FTIR Spectrum of carbon nanostructures (LA400) derived from low-grade coal lignite after annealing at a temperature of 400°C

The FTIR spectrum (Figure 20) have prominent peaks at 3218 cm^{-1}, 3345 cm^{-1}, 1579 cm^{-1}, and 1103 cm^{-1}. The 3218 cm^{-1} peak arises from the OH group of alcohols, carboxylic groups, and absorbed water. The nitrogen group (NH_2) peak (3345 cm^{-1}) is probably originated from lignite or during HNO_3 oxidation, which acts as a doping agent of nitrogen into carbon nanostructures. The band at 1579 cm^{-1} is originated from the conjugated C=C stretching vibration & carbonyl groups present in the nanocarbon. Finally, the peaks at 1103 cm^{-1} arise from C-O stretching (Kumar Thyagarajan et al., 2016).

Raman spectrum of carbon nanostructures (LA400) derived from low-grade coal lignite after annealing at a temperature of 400°C are presented in Figure 21.

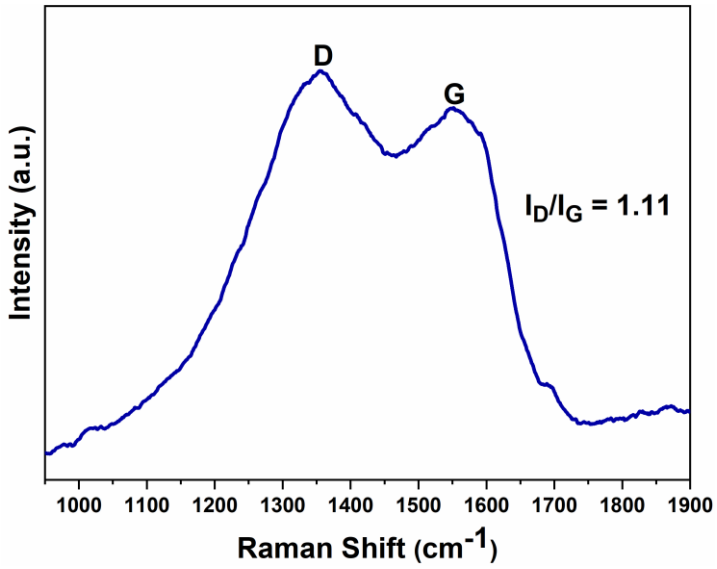

Figure 21: Raman spectrum of carbon nanostructures (LA400) derived from low-grade coal lignite after annealing at a temperature of 400°C

The spectrum revealed the existence of defect D band at ~1354 cm^{-1} and graphitic G band at ~1548 cm^{-1}. The D band is created by the momentum conservation law due to the formation of edge states (zigzag and armchair) and the G band is produced by the in-plane vibrations of sp^2 carbon (E_{2g} mode). The annealing of the coal at 400°C resulted in an increase of intensity of D peak and intensity of D peak became stronger than G peak. When the coal was annealed, the I_D/I_G ratio increased to 1.11 indicating that annealing increased the sp^2 content, localization length and density of edge-plane-like defective sites on coal, which may provide many active sites for electron transfer to electro active species and result in significantly increased electro catalytic activity. In conclusion, with excellent electrochemical properties predicted by raman spectra, the annealed coal may be used as a good alternative material for some well-known carbon materials (such as graphene and carbon nanotube, etc.) in electrochemical sensing (Huang et al., 2017).

4.3.2. Morphological analysis of the lignite derived carbon nanostructures

The surface morphology of the as-synthesized carbon nanostructures synthesized at 400°C is depicted in Figure 22.

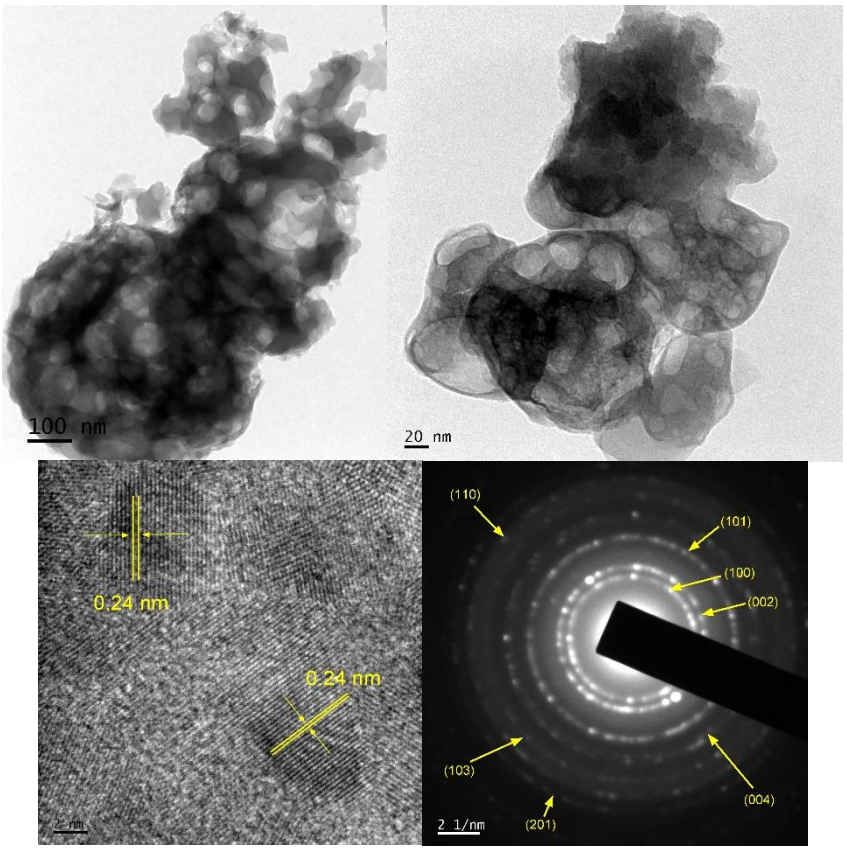

Figure 22: HRTEM images of the as-synthesized carbon nanostructures after annealing at 400 °C (LA400) portraying highly crystalline, microporous and mesoporous graphitic structure.

HRTEM images reveal that annealing at a higher temperature and oxidation process resulted in an increase in the percentage of micropores/mesopores. The disordered meso/micropores and carbon-channels observed provide a path for transportation of electrolyte ions as well as the occurrence of a redox reaction. The existence of combined micro-mesopores provide efficient mass transport pathways for the reaction between the nanostructure and heavy metal ions(Das et al., 2017). The lattice spacing is measured from the HRTEM image and is found to be 0.24 nm suggesting the crystalline nature of LA400. The corresponding SAED pattern shows a highly polycrystalline nature with (100), (002), (101), (004), (103), (110), and (201) planes of graphitic carbon.

4.3.3. Simultaneous electrochemical sensing of heavy metal ions cadmium and lead using the as-synthesized carbon nanostructures modified glassy carbon electrode

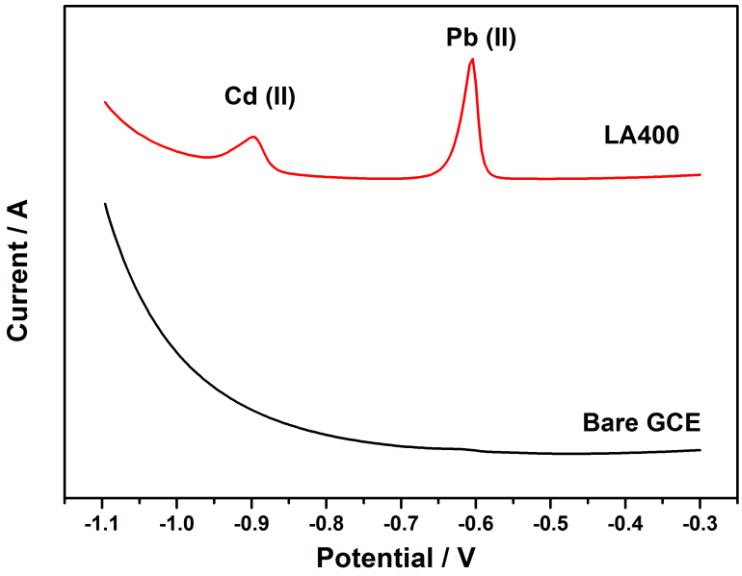

Figure 23: SWASVs for 13 µM each of Cd (II)and Pb (II) on bare (black line) and LA400 modified GCE (red line)

Figure 23 presents the Square Wave Anodic Stripping Voltammetry (SWASV) analytical characteristics of bare and LA400 modified GCE. When the accumulation process was carried out for 50 s at -0.7 V in a solution containing 13 µM each of Cd (II) and Pb (II) in 1 M HCl without deaeration, nearly no peaks at bare (black line) and sharper and higher peak current for the two target metal ions were obtained at the LA400 modified GCE (red line) in the potential range of -1.1 to -0.3 V. The increase in stripping currents at this modified electrode demonstrates that the LA400 modified GCE is very suitable for the accumulation process of Cd (II) and Pb (II) on the electrode surface (Individually, Cd (II) and Pb (II) can be identified at potentials of -0.86 and -0.57 V, respectively), resulting in increased sensitivity.

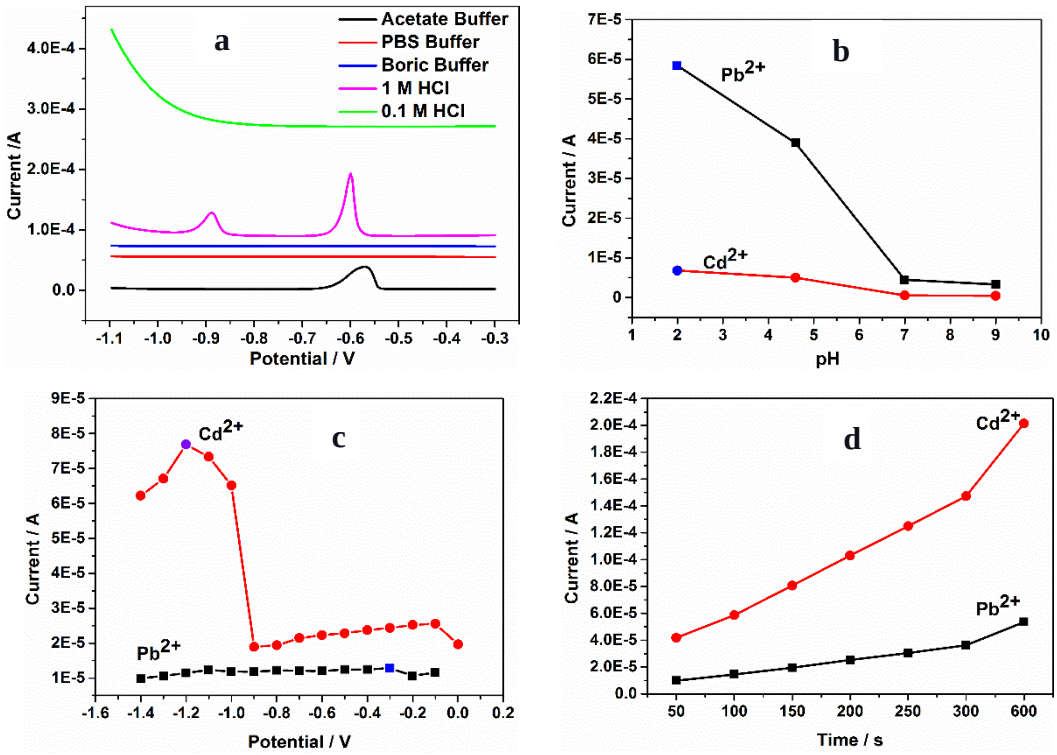

Figure 24: Optimization of Experimental Conditions. Influence of a) Supporting electrolytes; b) pH value; c) Deposition potential; and d) Deposition time on the voltammetry response

In order to get the maximum sensitivity for trace heavy metal detection LA400 modified GCE, the voltammetry parameters (supporting electrolytes, pH value, deposition potential, and deposition time) were optimized in a solution containing 1 µM each of Cd (II) and Pb (II).

Figure 24a reveals the voltammetry behaviour to two target metal ions, Cd (II) and Pb (II), in five different supporting electrolytes: acetate buffer, phosphate buffer, boric buffer, 1 M HCl, and 0.1 M HCl. Only one peak was observed in acetate buffer solution; the peak of Cd (II) could not be observed. Likewise, no peaks are observed in phosphate buffer, boric buffer, and 0.1 M HCl. However, well-defined voltammetry peak shapes are observed for Cd (II) and Pb (II) metal ions in 1 M HCl solution.

The pH value effect is significant and essential to select a proper pH value. Therefore, the effect of pH on the voltammetry response was investigated in the pH range 2.0 to 9.0. As shown in Figure 24b, the peak current for Cd (II) and Pb (II) decreased as the pH was changed from 2.0 to 9.0. The decrease of the stripping signal for Cd (II) and Pb (II) may be related with the hydrolysis of metal ions. Thus, a pH of 2.0 was selected for stripping measurements.

In stripping analysis, applying adequate deposition potential is very important to achieve the best sensitivity. Thus, the effect of the deposition potential on the peak current after 50 s accumulation was studied in the potential range from 0 to -1.4 V in 1M HCl solution. The obtained results are shown in Figure 23c. The highest current was obtained at a deposition potential of -1.2 V for Cd (II) and -0.3 V for Pb (II). Although a higher peak current for Cd (II) was obtained at an even more negative potential at -1.2 V, to avoid the competitive generation of H_2 and the co-deposition of other metal ions from analysis of real-life samples, we choose -0.7 V as the optimal deposition potential for the subsequent experiment.

As the deposition time can affect the detection limit and the sensitivity, different deposition times were studied in this work. The dependence of peak currents on the deposition time for two target metal ions is depicted in Figure 24d, the response of the stripping peak currents of Cd (II) and Pb (II) enhanced with the increase of the deposition time varying from 50 s up to 600 s, this is due to the increased amount of analytes on the modified electrode surface. Although increasing the deposition time improves the sensitivity, it also lowers the upper detection limit due to the surface saturation at high metal ions concentrations. Therefore, to achieve a lower detection limit and more comprehensive response range, 50 s was chosen as the deposition time.

Under the optimal experimental conditions, Cd (II) and Pb (II) were determined individually and simultaneously at the LA400 modified GCE using SWASV.

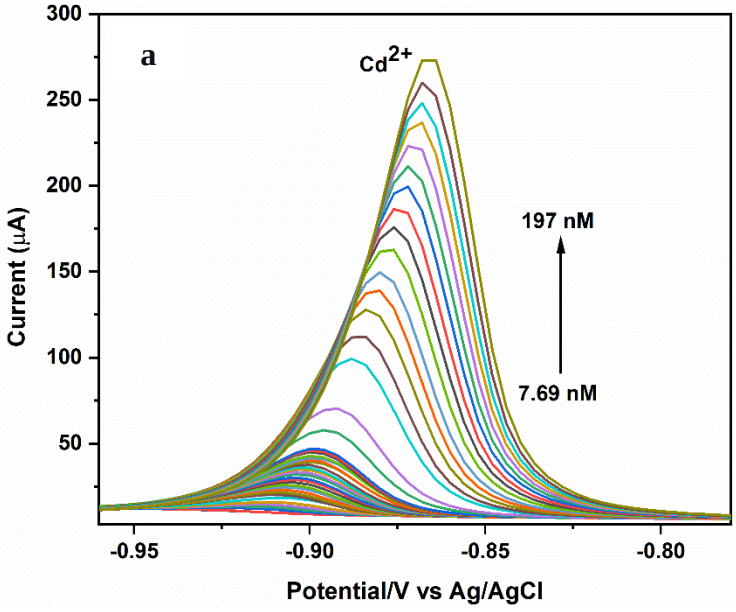

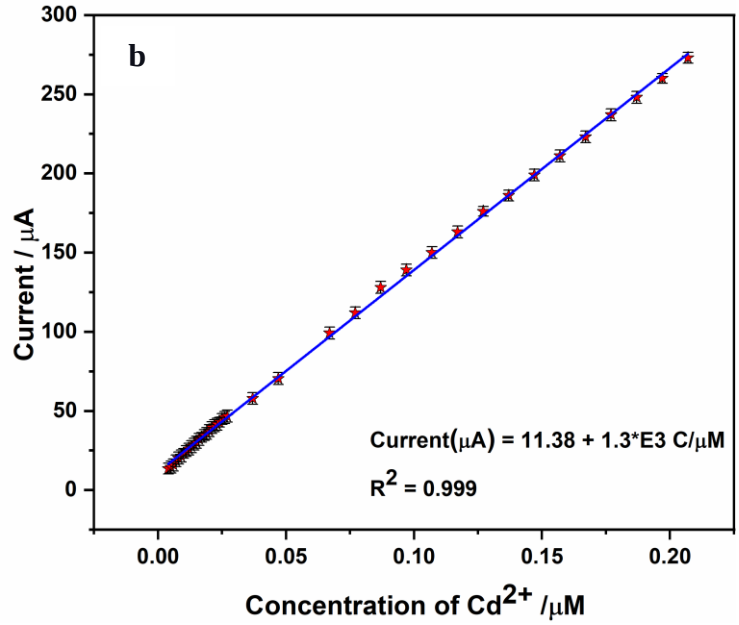

Figure 25: a) Square Wave Anodic Stripping Voltammetry (SWASV) response of LA400 modified GCE for the individual analysis of Cd (II) over a concentration range of 7.69 to 197 nM and b) linear calibration plot of peak current against Cd (II) concentration. Modified GCE in 1 M HCl. deposition potential - -0.3 V; deposition time- 50 s; amplitude, 25 mV; increment potential, 4 mV; frequency, 15 Hz; vs Ag/AgCl.

Figure 25a shows the SWASV responses toward Cd (II) at different concentrations. Well-defined peaks, proportional to Cd (II) concentration, were observed in the range of 7.69 to 197 nM. The values of the limit of detection (LOD) and limit of quantification (LOQ) were calculated using statistical formulae (3.3σ/S) and (10σ/S) respectively (Yahyazadeh & Shemirani, 2019), where σ signifies standard deviation of the y-intercept and S denotes the slope of calibration plot. The linearization equation is Current(A) = 11.38 + 1.3E3 C/µM, with the correlation coefficients of 0.999 (Figure 25b). The limit of detection (LOD) and limit of quantification (LOQ) was calculated to be 2.54 nM and 7.69 nM, respectively. As the ion concentration increased, the anodic peak potential shifted towards more positive potential due to the positive electrocatalytic activity of the heavy metal ions with the electrode. This phenomenon of peak shift is common as adsorption product tends to shift the peak potential positively.

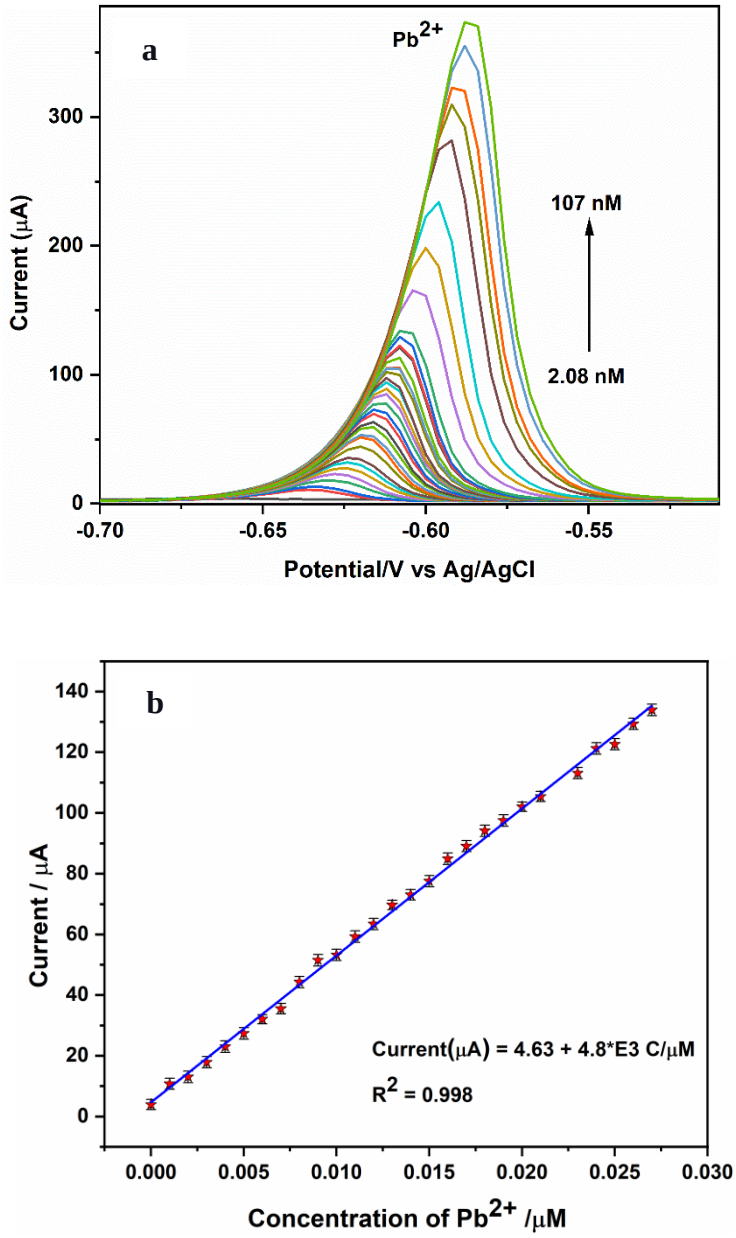

Figure 26: a) Square Wave Anodic Stripping Voltammetry (SWASV) response of LA400 modified GCE for the individual analysis of Pb (II) over a concentration range of 2.08 to 107 nM and b) linear calibration plot of peak current against Pb (II) concentration. Modified GCE in 1 M HCl. deposition potential - -0.85 V; deposition time- 60 s; amplitude, 25 mV; increment potential, 4 mV; frequency, 15 Hz; vs Ag/AgCl.

The SWASV responses of the LA400 modified GCE toward Pb (II) over a concentration range of 2.08 to 107 nM are shown in Figure 26a. The linearization equation is Current(A) = 4.63 + 4.8E3 C/ μM, with the correlation coefficient of 0.998

(Figure 26b). The limit of detection (LOD) and limit of quantification (LOQ) was calculated as 0.68 nM and 2.08 nM, respectively.

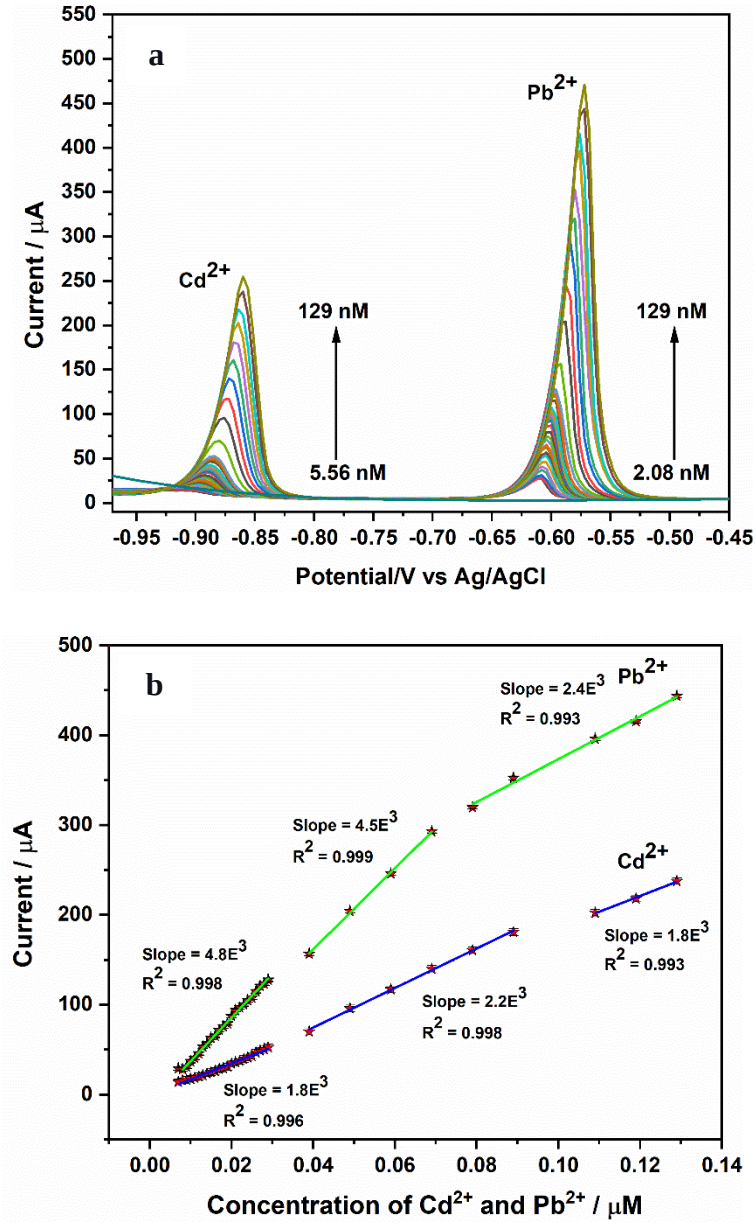

Figure 27: a) Square Wave Anodic Stripping Voltammetry (SWASV) response of LA400 modified GCE for the simultaneous analysis of Cd (II) and Pb (II) over a concentration range of 5.56 to 129 nM and 2.08 to 129 nM respectively b) The respective calibration curves of Cd (II) and Pb (II) corresponding to panel a. Modified GCE in 1 M HCl. deposition potential - -0.7 V; deposition time- 50 s; amplitude, 25 mV; increment potential, 4 mV; frequency, 15 Hz; vs. Ag/AgCl.

When analysing the SWASV responses of the LA400 modified GCE toward the simultaneous detection of Cd (II) and Pb (II), as shown in Figure 27a, well-defined

peaks of Cd (II) and Pb (II) were observed. As shown in Figure 27b, a unique triple linear detection range can be observed over the concentration ranges 2.08 to 129 nM and 5.56 to 129 nM for Cd (II) and Pb (II), respectively with LOD calculated to be 1.83 nM, 1.5 nM and 1.83 nM for Cd (II) from the three linear ranges and 0.68 nM, 0.73 nM and 1.38 nM for Pb (II) from the three linear ranges.

The shift in linearity can be connected to the kinetics of the electrochemical reaction. The reason behind the existence of multiple linear ranges can be derived from the structural properties of pores, including structural defects on the surface (geometrical), the chemical disorder in the pore system, as well as the surface heterogeneity and surface diffusivity that play an essential role in the transport kinetics of heavy metals inside a porous material where adsorption is the primary mechanism. The sorption and penetration of heavy metal molecules into the pore system of combined micro-mesopores is primarily accomplished by filling finer and wider micropores. Fluid phase diffusion mainly contributes to the overall diffusion kinetics. The filling of finer and wider mesopores will completely cover the monolayer where the diffusion rate is at its maximum due to stochastic molecular ballistic flights (Knudsen flights). They experience ballistic flights until they get adsorbed by colliding with the pore wall. Fast transport times and better detection at low concentrations may have been caused by these factors, as well. At higher concentrations of heavy metal ions, a multi-layering of adsorbate on opposite pore walls reduces the effective pore size. As a result, larger quantities of pores are increasingly filled, and a relatively lower number of molecules are present in the adsorbed phase compared to that in the fluid phase. Finally, molecular flights are less common, which is attributed to the increased tortuosity.

Furthermore, molecular uptake is progressively retarded, which is associated with the rearrangement of molecular ensembles, e.g., between adjacent constrictions in the pore space, rather than with the rearrangement of individual molecules. This could explain the decrease in sensitivity in electrochemical detection at higher concentrations of heavy metals (Zeinu et al., 2016).

4.3.3.1. Repeatability and reproducibility

The repeatability of the LA400 modified GCE electrode for Cd (II), and Pb (II) determination was studied by duplicating the experiment with standard solutions of Cd (II) and Pb (II) five times. Furthermore, the relative standard deviation (RSD) value for LA400 modified GCE electrode towards the reduction of Cd (II), and Pb (II) was within

limits (less than 0.4%). The reproducibility of the response of the LA400 modified GCE electrode was studied. The RSD value was less than 0.4 % to determine Cd (II) and Pb (II). The results have shown acceptable repeatability and reproducibility for LA400 modified GCE electrode towards Cd (II) and Pb (II) analysis.

4.3.3.2. Selectivity and interference

Selectivity is one of the critical indexes to judge the reliability of a sensor for practical applications. Selectivity tests were conducted by recording SWASVs for the detection of Cd (II) and Pb (II) at the LA400 modified GCE electrode in the presence of some interfering agents potassium (K^+), nickel (Ni^{2+}), calcium (Ca^{2+}), magnesium (Mg^{2+}), ferrous (Fe^{3+}), sodium (Na^+), manganese (Mn^{2+}), mercury (Hg^{2+}), and copper (Cu^{2+}).

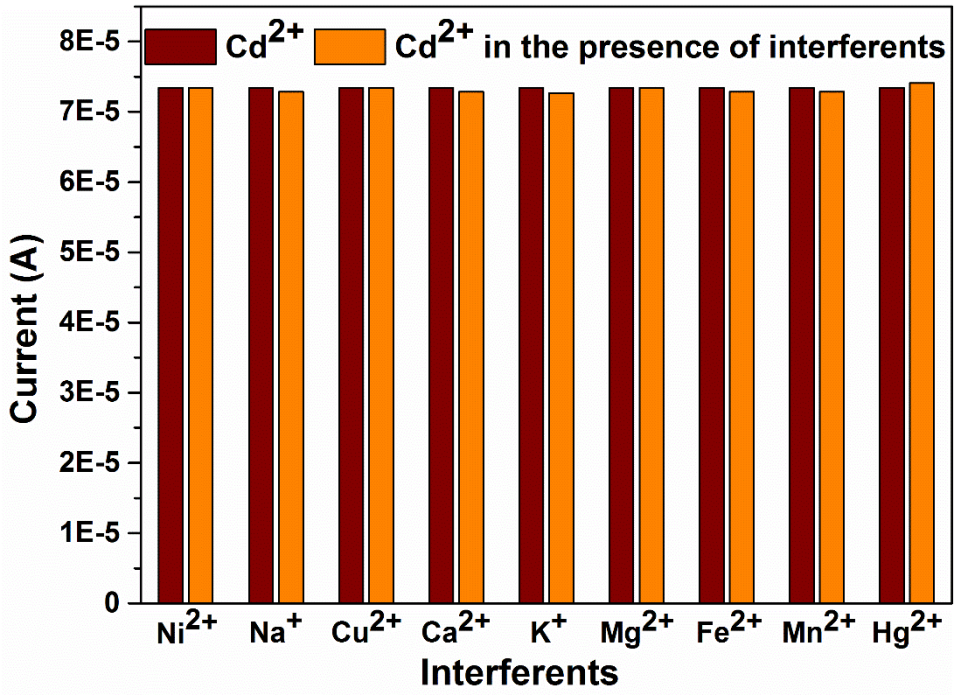

Figure 28a: SWASV response of the Cd^{2+} sensing of LA400 modified GCE electrode in the presence of a number of interfering agents in 1 M HCl

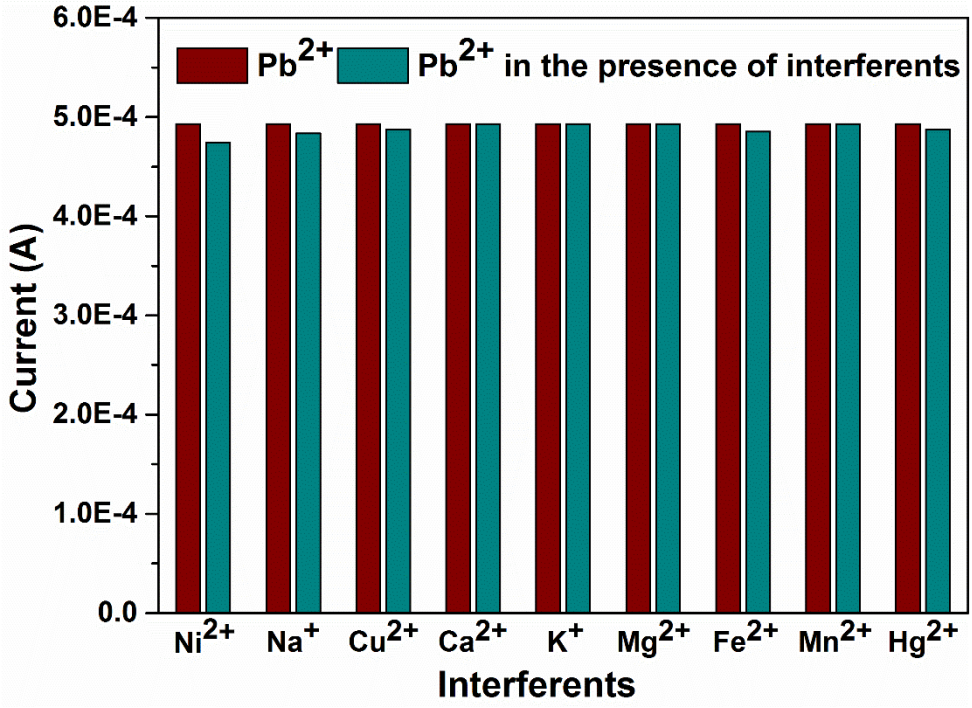

Figure 28b: SWASV response of the Pb^{2+} sensing of LA400 modified GCE electrode in the presence of a number of interfering agents in 1 M HCl

Figure 28a and 28b reveals that the current signal of Cd (II) and Pb (II) is negligibly influenced by interfering ions. These results suggest that the specific binding of the recognition layer of LA400 with cadmium and lead ions is much stronger than the nonspecific binding with interfering agents.

4.3.3.3. Determination of Cd (II) and Pb (II) in real samples

The applicability of the proposed method was evaluated by determining Cd (II) and Pb (II) in lake water and tap water samples. Cd (II) and Pb (II) contents in these samples were quantified by employing standard addition method using SWASV technique. The spiked samples of Cd (II) and Pb (II) were diluted with PBS (pH 7.0) and only suitable amounts were used for the determination of Cd (II) and Pb (II). A reduction peak of Cd (II) and Pb (II) was significantly observed around -0.86 and -0.57 V potential corresponding to Cd (II) and Pb (II) on the square wave anodic stripping voltammograms for both the real samples. The results substantiate the efficiency of the proposed method in the quantitative determination of Cd (II) and Pb (II) in real samples (Table 5). The recovery values were observed between 98.25% and 102.75% with a minimum RSD value.

Table 5: Analysis of Cd (II) and Pb (II) content in spiked lake water and tap water

Sensor	Formulation	Cd (II) and Pb (II)

		Spiked (nM)	Found (nM)	RSD (%)	Recovery (%)
LA400 modified GCE	Pb (II) in Lake Water	8	8.21	0.37	102.62
		16	16.14	0.39	100.87
		24	23.87	0.40	99.46
	Pb (II) in Tap Water	8	8.22	0.37	102.75
		16	15.72	0.36	98.25
		24	23.82	0.40	99.25
LA400 modified GCE	Cd (II) in Lake Water	8	8.12	0.38	101.54
		16	15.81	0.39	98.81
		24	23.87	0.37	99.46
	Cd (II) in Tap Water	8	8.18	0.40	102.3
		16	15.8	0.40	98.75
		24	23.83	0.40	99.29

4.3.4. Conclusion

In the present study, using LA400 nanoparticles modified GCE electrode for the simultaneous electrochemical determination of Cd (II) and Pb (II) is reported. Here, the edge plane sites are the principal location for electron transfer arising from oxygen functionalities on active sites. Edge plane sites on the surface improved electron transfer kinetics and also increased resistance to surface passivation. The enhanced electrochemical properties could also be attributed to its lower charge transfer resistance. The voltammetry peak for the stripping of Cd (II) and Pb (II) on the LA400 modified GCE electrode appears at different potentials with a separation of 290 mV between the stripping peaks. The described electrode can be used for the simultaneous detection of two heavy metals with very low interference effects, with a high stability and a long-term usage possibility. The obtained LOD is very well below the guideline value given by the World Health Organization (WHO). Hence, these results suggest that LA400 modified GCE electrode is a promising material in electrochemically detecting heavy metal ions.

The study pertaining to this is being communicated in the journal "Environmental Pollution" titled as "Exploration of the potential efficacy of lignite derived carbon nanostructure for the simultaneous electrochemical detection of cadmium and lead".

5. SUMMARY AND FUTURE PROSPECTS

In summary, facile, economic, efficient, scalable synthesis techniques to produce carbon nanostructures using low grade coal lignite, namely, for copper ion fluorescence sensing, glucose fluorescence sensing, and electrochemical sensing of heavy metal ions applications, have been established in the current study.

Carbon nanostructures (LC1, LC2 and LC3) with varying structures, compositions, morphologies, and optical properties are produced in the present work utilizing dialysis separation technique from low-grade coal lignite, and the as-synthesized carbon nanostructures demonstrated excellent fluorescence characteristics. They exhibited remarkable copper ion sensing with a dual linear range with limits of detection (LOD) as low as 1.32 pM and 2.35 pM, and limits of quantification (LOQ) as low as 4 pM and 7.14 pM. The recovery rates of copper ions ranged from 98.18% to 101.2%, with Relative Standard Deviations (RSDs) of less than 0.4%, indicating the accuracy of the fabricated sensor. The results are captivating, implying that these lignite derived carbon nanostructures based copper ions sensing could be employed to efficiently and economically detect low concentrations of copper ions.

Carbon nanostructures (LR100, LR150, and LR200) with various structures, compositions, morphologies, and optical properties are synthesized from low-grade coal lignite by altering the synthesis temperature. The acidic-oxidized carbon nanostructures exhibited relatively enhanced optical behavior and sensing performance. It demonstrated excellent quantum yield, a fluorescence lifetime of ~4.98 ns, fluorescence detection of glucose with high quenching efficiency and a limit of detection as low as 3.3 µM, best suited for precise quantification of glucose in actual samples, with significant potential for implementation in diabetes management.

An efficient electrode material (LA400) was synthesized from low grade coal, lignite and utilized for the simultaneous electrochemical determination of Cd (II) and Pb (II). The study shows an electrochemical performance comparable to graphene and expands the utility of lignite. One of the key steps in the synthesis of these carbon nanostructures is the annealing of lignite at 400°C, which results in a large number of edge-plane-like defects and low charge transfer resistance, resulting in high electron transfer efficiency and excellent electro catalytic activity, making it a promising signal amplifier material and modified matrix for electrochemical sensing. The voltammetry peak for the stripping of Cd (II) and Pb (II) on the LA400 modified GCE electrode appears at different potentials with a separation of 290 mV between the stripping peaks.

With very low interference effects, these ions can be reliably determined simultaneously. The obtained LOD is very well below the guideline value given by the World Health Organization (WHO).

The scope of future work involves the achievement of precise control of the particle size and surface chemistry of lignite derived carbon nanostructures, detailed study of origin of fluorescence, enhancement of fluorescence quantum yield by edge modification, enrichment of the structure electron density through reduction, & suppression of non-radiative recombination by removing the epoxy groups and enhancement of the sensing performance of as-synthesized carbon nanostructures by optimizing various parameters to increase the sensing specificity which would lead to more developments in the commercialization of coal-based CNs.

6. STRUCTURE OF THE THESIS

The thesis would be structured to include seven chapters. Chapter 1 would comprise a detailed introduction to the carbon nanostructures including their preparation, properties, and applications, in relevance with the current study, and significance of coal as a precursor among other expensive precursors. Chapter 2 would be devoted to reviewing the existing literature outlining the evolution and applicability of the carbon nanostructures with respect to the current research. An overview of the research methodology adopted for the current work would be presented in Chapter 3. Chapter 4 would elaborate on the fabrication and investigation of the fluorescence properties of carbon nanostructures derived from low grade coal, lignite for copper ion sensing. The synthesis, characterization, and selective fluorescence detection of glucose by the as-synthesized carbon nanostructures obtained from low grade coal, lignite would be presented in Chapter 5. Chapter 6 would discuss the preparation and analyses of the carbon nanostructures derived from low grade coal, lignite for electrochemical sensing of heavy metal ions cadmium and lead. Finally, Chapter 7 would present a detailed summary and logical conclusions derived from the current work along with a glimpse of the scope for future work.

BIBLIOGRAPHY

Anas, N. A. A., Fen, Y. W., Omar, N. A. S., Daniyal, W. M. E. M. M., Ramdzan, N. S. M., & Saleviter, S. (2019). Development of graphene quantum dots-based optical sensor for toxic metal ion detection. *Sensors*, *19*(18), 1–30. https://doi.org/10.3390/s19183850

Awasthi, S., Awasthi, K., Ghosh, A. K., Srivastava, S. K., & Srivastava, O. N. (2015). Formation of single and multi-walled carbon nanotubes and graphene from Indian bituminous coal. *Fuel*, *147*, 35–42. https://doi.org/10.1016/j.fuel.2015.01.043

Baker, S. N., & Baker, G. A. (2010). Luminescent carbon nanodots: Emergent nanolights. *Angewandte Chemie - International Edition*, *49*(38), 6726–6744. https://doi.org/10.1002/anie.200906623

Balachandran, M. (2014). Role of Infrared Spectroscopy in Coal Analysis — An Investigation. *American Journal of Analytical Chemistry*, *April*, 367–372. https://doi.org/10.4236/ajac.2014.56044

Bijiang Geng, Dewen Yang, Fengfeng Zheng, Chen Zhang, Jing Zhan, Zhen Li, a D., & Wang, P. and L. (2017). Facile Conversion of Coal Tar to Orange Fluorescent Carbon Quantum Dots and Their Composite Encapsulated by Liposomes for Bioimaging. *New Journal of Chemistry*, *41*, 14444–14451. https://doi.org/10.1039/C7NJ03005C

Brainina, K. Z., Stozhko, N. Y., Belysheva, G. M., Inzhevatova, O. V., Kolyadina, L. I., Cremisini, C., & Galletti, M. (2004). Determination of heavy metals in wines by anodic stripping voltammetry with thick-film modified electrode. *Analytica Chimica Acta*, *514*(2), 227–234. https://doi.org/10.1016/j.aca.2004.03.047

Chang, H., Hsiao, W. W.-W., & Su, M. (2007). Fluorescent nanodiamonds. In *Wiley* (Vol. 62, Issue 11). https://doi.org/10.1016/s0026-0657(07)70221-7

Chansaenpak, K., Kamkaew, A., Lisnund, S., Prachai, P., & Ratwirunkit, P. (2021). Development of a Sensitive Self-Powered Glucose Biosensor Based on an Enzymatic Biofuel Cell. *BIOSENSORS*, *11*(1), 16.

Chen, C., Xie, Q., Yang, D., Xiao, H., Fu, Y., Tan, Y., & Yao, S. (2013). Recent advances in electrochemical glucose biosensors: A review. *RSC Advances*, *3*(14), 4473–4491. https://doi.org/10.1039/c2ra22351a

Chingombe, P., Saha, B., & Wakeman, R. J. (2005). Surface modification and characterisation of a coal-based activated carbon. *Carbon*, *43*, 3132–3143. https://doi.org/10.1016/j.carbon.2005.06.021

Choudhary, M., Shukla, S. K., Taher, A., Siwal, S., & Mallick, K. (2014). Organic-inorganic hybrid supramolecular assembly: An efficient platform for nonenzymatic glucose sensor. *ACS Sustainable Chemistry and Engineering*, *2*(12), 2852–2858. https://doi.org/10.1021/sc500613q

Claramunt, S., Varea, A., López-Díaz, D., Velázquez, M. M., Cornet, A., & Cirera, A. (2015). The importance of interbands on the interpretation of the raman spectrum of graphene oxide. *Journal of Physical Chemistry C*, *119*(18), 10123–10129. https://doi.org/10.1021/acs.jpcc.5b01590

Dai, X., Qiu, F., Zhou, X., Long, Y., Li, W., & Tu, Y. (2014). Amino-functionalized mesoporous silica modified glassy carbon electrode for ultra-trace copper(II) determination. *Analytica Chimica Acta*, *848*(Ii), 25–31. https://doi.org/10.1016/j.aca.2014.08.002

Danielle Bruen, Colm Delaney, L. F. and D. D. I. (2017). Glucose Sensing for Diabetes Monitoring : Recent Developments. *Sensors*, *17*, 1866. https://doi.org/10.3390/s17081866

Das, T., Chauhan, H., Deka, S., Chaudhary, S., Boruah, R., & Saikia, B. K. (2017). Promising carbon nanosheet-based supercapacitor electrode materials from low-grade coals. *Microporous and Mesoporous Materials*, *253*, 80–90. https://doi.org/10.1016/j.micromeso.2017.06.030

Ding, H., Li, X.-H., Chen, X.-B., Wei, J.-S., Li, X.-B., & Xiong, H.-M. (2020). Surface states of carbon dots and their influences on luminescence Surface states of carbon dots and their influences on luminescence. *Phys, J Appl*, *127*, 231101. https://doi.org/10.1063/1.5143819

Dong, Y., Lin, J., Chen, Y., Fu, F., Chi, Y., & Chen, G. (2014). Graphene quantum dots, graphene oxide, carbon quantum dots and graphite nanocrystals in coals. *Nanoscale*, *6*, 7410–7415. https://doi.org/10.1039/c4nr01482k

Ferri, S., Kojima, K., & Sode, K. (2011). Review of Glucose Oxidases and Glucose Dehydrogenases: A Bird's Eye View of Glucose Sensing Enzymes. *Journal of Diabetes Science and Technology*, *5*, 1068. https://doi.org/10.1177/193229681100500507

Ghosh, J., Ghosh, R., & Giri, P. K. (2018). Sensors and Actuators B : Chemical Tuning the visible photoluminescence in Al doped ZnO thin film and its application in label-free glucose detection. *Sensors & Actuators: B. Chemical*, *254*, 681–689. https://doi.org/10.1016/j.snb.2017.07.110

Grayfer, E. D., Nazarov, A. S., Makotchenko, V. G., Kim, S. J., & Fedorov, V. E. (2011). Chemically modified graphene sheets by functionalization of highly exfoliated graphite. *Journal of Materials Chemistry*, *21*, 3410–3414. https://doi.org/10.1039/c0jm02469d

Hoang, V. C., Hassan, M., & Gomes, V. G. (2018). Coal derived carbon nanomaterials – Recent advances in synthesis and applications. *Applied Materials Today*, *12*, 342–358. https://doi.org/10.1016/j.apmt.2018.06.007

Hu, C., Yu, C., Li, M., Wang, X., Yang, J., & Zhao, Z. (2014). Chemically Tailoring Coal to Fluorescent Carbon Dots with Tuned Size and Their Capacity for Cu (II) Detection. *Small*, *10*, 4926–4933. https://doi.org/10.1002/smll.201401328

Hu, S., Tian, F., Bai, P., Cao, S., Sun, J., & Yang, J. (2009). Synthesis and luminescence of nanodiamonds from carbon black. *Materials Science and Engineering B: Solid-State Materials for Advanced Technology*, *157*(1–3), 11–14. https://doi.org/10.1016/j.mseb.2008.12.001

Hu, S., Wei, Z., Chang, Q., Trinchi, A., & Yang, J. (2016). A facile and green method towards coal-based fluorescent carbon dots with photocatalytic activity. *Applied Surface Science*, *378*, 402–407. https://doi.org/10.1016/j.apsusc.2016.04.038

Huang, J., Zeng, Q., Bai, S., & Wang, L. (2017). Application of Coal in Electrochemical Sensing. *Analytical Chemistry*, *89*(16), 8358–8365. https://doi.org/10.1021/acs.analchem.7b01612

Jahandari, S., Taher, M. A., Fazelirad, H., & Sheikhshoai, I. (2013). Anodic stripping voltammetry of silver(I) using a carbon paste electrode modified with multi-walled carbon nanotubes. *Microchimica Acta*, *180*(5–6), 347–354. https://doi.org/10.1007/s00604-012-0935-x

Jaishankar, M., Tseten, T., Anbalagan, N., Mathew, B. B., & Beeregowda, K. N. (2014). Toxicity , mechanism and health effects of some heavy metals. *Interdisciplinary Toxicology*, *7*(2), 60–72. https://doi.org/10.2478/intox-2014-0009

Jayaweera, S., Yin, K., Hu, X., & Ng, W. J. (2019). Facile preparation of fluorescent carbon dots for label-free detection of Fe3+. *Journal of Photochemistry and Photobiology A: Chemistry*, *370*, 156–163. https://doi.org/10.1016/j.jphotochem.2018.10.052

Jung, H. S., Cho, K. J., Ryu, S. J., Takagi, Y., Roche, P. A., & Neuman, K. C. (2020). Biocompatible Fluorescent Nanodiamonds as Multifunctional Optical Probes for Latent Fingerprint Detection. *ACS Applied Materials and Interfaces*, *12*(5), 6641–6650. https://doi.org/10.1021/acsami.9b19245

Kaniyoor, A., & Ramaprabhu, S. (2012). A Raman spectroscopic investigation of graphite oxide derived graphene. *AIP Advances*, *2*, 032183. https://doi.org/10.1063/1.4756995

Katalambula, H., & Gupta, R. (2009). Low-Grade Coals : A Review of Some Prospective Upgrading. *Energy and Fuels*, *23*, 3392–3405.

Kovalchuk, A., Huang, K., Xiang, C., Martí, A. A., & Tour, J. M. (2015). Luminescent Polymer Composite Films Containing Coal-Derived Graphene Quantum Dots. *ACS Applied Materials and Interfaces*, *7*, 26063–26068. https://doi.org/10.1021/acsami.5b06057

Kumar Thiyagarajan, S., Raghupathy, S., Palanivel, D., Raji, K., & Ramamurthy, P. (2016). Fluorescent carbon nano dots from lignite: unveiling the impeccable evidence for quantum confinement. *Physical Chemistry Chemical Physics*, *18*(17), 12065–12073. https://doi.org/10.1039/C6CP00867D

Li, G., Ji, Z., & Wu, K. (2006). Square wave anodic stripping voltammetric determination of Pb2+ using acetylene black paste electrode based on the inducing adsorption ability of I-. *Analytica Chimica Acta*, *577*(2), 178–182. https://doi.org/10.1016/j.aca.2006.06.061

Li, K., Liu, W., Ni, Y., Li, D., Lin, D., Su, Z., & Wei, G. (2017). Technical synthesis and biomedical applications of graphene quantum dots. *Journal of Materials Chemistry B*, *5*(25), 4811–4826. https://doi.org/10.1039/c7tb01073g

Li, M., Ge, H., Arrowsmith, R. L., Mirabello, V., Zhu, S. W. B. W., Pascu, S. I., & James, T. D. (2014). Ditopic boronic acid and imine-based naphthalimide fluorescence sensor for copper(II). *Chemical Communications*, *50*, 11806–11809. https://doi.org/10.1039/b000000x

Li, M., Yu, C., Hu, C., Yang, W., Zhao, C., Wang, S., Zhang, M., Zhao, J., Wang, X., & Qiu, J. (2017). Solvothermal conversion of coal into nitrogen-doped carbon dots with singlet oxygen generation and high quantum yield. *Chemical Engineering Journal*, *320*, 570–575. https://doi.org/10.1016/j.cej.2017.03.090

Liu, M. (2020). Optical Properties of Carbon Dots: A Review. *Nanoarchitectonics*, *1*(1), 1–12. https://doi.org/10.37256/nat.112020124.1-12

Liu, Xuexia , Hao, a, Jianhui Liu, b, H. T. (2018). Green synthesis of carbon quantum dots from lignite coal and the application in Fe3+ detection. *IOP Conference Series :Earth and Environmental Science*, *113*, 012063.

Lueking, A. D., Gutierrez, H. R., Jain, P., Van Essandelft, D. T., & Burgess-Clifford, C. E. (2007). The effect of HCl and NaOH treatment on structural transformations in a ball-milled anthracite after thermal and chemical processing. *Carbon*, *45*(11), 2297–2306. https://doi.org/10.1016/j.carbon.2007.04.027

Mano, N. (2019). Engineering glucose oxidase for bioelectrochemical applications. *Bioelectrochemistry*, *128*, 218–240.

Manoj, B., Raj, A. M., & Chirayil, G. T. (2017). Tunable direct band gap photoluminescent organic semiconducting nanoparticles from lignite. *Scientific Reports*, *7*(April), 18012. https://doi.org/10.1038/s41598-017-18338-2

Manoj, B., Raj, A. M., & Chirayil, G. T. (2018). Facile synthesis of preformed mixed nano-carbon structure from low rank coal. *Materials Science- Poland*, *36*, 14–20. https://doi.org/10.1515/msp-2018-0026

Manoj, B., Raj, A. M., & Thomas, G. C. (2018). Tailoring of low grade coal to fluorescent nanocarbon structures and their potential as a glucose sensor. *Scientific Reports*, *8*, 1–9. https://doi.org/10.1038/s41598-018-32371-9

Mendes, R. G., Wróbel, P. S., Bachmatiuk, A., Sun, J., Gemming, T., Liu, Z., & Rümmeli, M. H. (2018). Carbon nanostructures as a multi-functional platform for sensing applications. *Chemosensors*, *6*(4), 60. https://doi.org/10.3390/chemosensors6040060

Moothi, K., Iyuke, S. E., Meyyappan, M., & Falcon, R. (2012). Coal as a carbon source for carbon nanotube synthesis. *Carbon*, *50*, 2679–2690. https://doi.org/10.1016/j.carbon.2012.02.048

Pang, L. S. K. (1993). Fullerenes from brown (lignite) coal. *Fuel Processing Technology*, *34*, 147–155. https://doi.org/10.1016/0378-3820(93)90097-N

Petit, T., & Puskar, L. (2018). FTIR spectroscopy of nanodiamonds: Methods and interpretation. *Diamond and Related Materials*, *89*(December 2017), 52–66. https://doi.org/10.1016/j.diamond.2018.08.005

Qin, Z. (2018). New advances in coal structure model. *International Journal of Mining Science and Technology*, *28*, 541–559. https://doi.org/10.1016/j.ijmst.2018.06.010

Rahman, M. R. U. (2017). Electrochemical Detection of Low-concentration Lead (II) Ions from Water. In *Dissertation* (Issue December).

Raj, A. M., & Balachandran, M. (2020). Coal-Based Fluorescent Zero-Dimensional Carbon Nanomaterials : A Short Review. *Energy and Fuels*, *34*(11), 13291–13306. https://doi.org/10.1021/acs.energyfuels.0c02619

Ramdass, A., Sathish, V., Babu, E., Velayudham, M., Thanasekaran, P., & Rajagopal, S. (2017). Recent Developments on Optical and Electrochemical Sensing of Copper (II) Ion Based on Transition Metal Complexes. *Coordination Chemistry Reviews*, *Ii*. https://doi.org/10.1016/j.ccr.2017.06.002

Ramya, A. V., Mohan, A. N., & Manoj, B. (2016). Wrinkled graphene: Synthesis and characterization of few layer graphene-like nanocarbons from kerosene. *Materials Science- Poland*, *34*, 330–336. https://doi.org/10.1515/msp-2016-0061

Rao, C. N. R., Sood, A. K., Subrahmanyam, K. S., & Govindaraj, A. (2009). Graphene: The new two-dimensional nanomaterial. *Angewandte Chemie - International Edition*, *48*(42), 7752–7777. https://doi.org/10.1002/anie.200901678

Rebelo, S. L. H., Guedes, A., Szefczyk, M. E., Pereira, A. M., Araújo, J. P., & Freire, C. (2016). Progress in the Raman spectra analysis of covalently functionalized multiwalled carbon nanotubes: Unraveling disorder in graphitic materials. *Physical Chemistry Chemical Physics*, *18*(18), 12784–12796. https://doi.org/10.1039/c5cp06519d

Rodrigues, S., Suárez-Ruiz, I., Marques, M., Flores, D., Camean, I., & García, A. B. (2011). Development of graphite-like particles from the high temperature treatment of carbonized anthracites. *International Journal of Coal Geology*, *85*, 219–226. https://doi.org/10.1016/j.coal.2010.11.007

Ruedas-rama, M. J., Camprubı, M., Lapresta-ferna, A., & Megia-ferna, A. (2013). Carbon dots for copper detection with down and upconversion fluorescent properties as excitation sources. *Chemical Communications*, *49*, 1103–1105. https://doi.org/10.1039/c2cc36450f

Sadezky, A., Muckenhuber, H., Grothe, H., Niessner, R., & Pöschl, U. (2005). Raman microspectroscopy of soot and related carbonaceous materials: Spectral analysis and structural information. *Carbon*, *43*(8), 1731–1742. https://doi.org/10.1016/j.carbon.2005.02.018

Saha, P., & Sarkar, S. (2019). Microbial Degradation of Coal into a Value Added Product. *International Journal of Coal Preparation and Utilization*, *39*(1), 1–19. https://doi.org/10.1080/19392699.2018.1448800

Saikia, M., Hower, J. C., Das, T., Dutta, T., & Saikia, B. K. (2019). Feasibility study of preparation of carbon quantum dots from Pennsylvania anthracite and Kentucky bituminous coals. *Fuel*, *243*, 433–440. https://doi.org/10.1016/j.fuel.2019.01.151

Savitskii, D. P. (2017). Preparation and characterization of colloidal dispersions of graphene-like structures from different ranks of coals. *Journal of Fuel Chemistry and Technology*, *45*(8), 897–907. https://doi.org/10.1016/s1872-5813(17)30043-9

Shang, J., Ma, L., Li, J., Ai, W., Yu, T., & Gurzadyan, G. G. (2012). The origin of fluorescence from graphene oxide. *Scientific Reports*, *2*, 1–8. https://doi.org/10.1038/srep00792

Shi, F., Cui, S., Liu, H., & Pu, S. (2020). Dyes and Pigments A high selective fluorescent sensor for Cu 2 þ in solution and test paper strips. *Dyes and Pigments*, *173*(July 2019), 107914. https://doi.org/10.1016/j.dyepig.2019.107914

Shinde, D. B., & Pillai, V. K. (2012). Electrochemical preparation of luminescent graphene quantum dots from multiwalled carbon nanotubes. *Chemistry - A European Journal*, *18*, 12522–12528. https://doi.org/10.1002/chem.201201043

Shuvo, M. A. I., Khan, M. A. R., Karim, H., Morton, P., Wilson, T., & Lin, Y. (2013). Investigation of modified graphene for energy storage applications. *ACS Applied Materials and Interfaces*, *5*, 7881–7885. https://doi.org/10.1021/am401978t

Sonthalia, P., McGaw, E., Show, Y., & Swain, G. M. (2004). Metal ion analysis in contaminated water samples using anodic stripping voltammetry and a nanocrystalline diamond thin-film electrode. *Analytica Chimica Acta*, *522*(1), 35–44. https://doi.org/10.1016/j.aca.2004.06.071

Su, D. S. (2009). The use of natural materials in nanocarbon synthesis. *Chemistry Sustainability Energy Materials*, *2*, 1009–1020. https://doi.org/10.1002/cssc.200900046

Sung, T., & Lo, Y. (2012). Sensors and Actuators B : Chemical Highly sensitive and selective sensor based on silica-coated CdSe / ZnS nanoparticles for Cu 2 + ion detection. *Sensors & Actuators: B. Chemical*, *165*(1), 119–125. https://doi.org/10.1016/j.snb.2012.02.028

Tam, T. van, & Choi, W. M. (2018). One-pot synthesis of highly fluorescent amino-functionalized graphene quantum dots for effective detection of copper ions. *Current Applied Physics*, *18*(11), 1255–1260. https://doi.org/10.1016/j.cap.2018.07.002

Treacy, M. M. J., Ebbesen, T. W., & Gibson, J. M. (1996). Exceptionally high Young's modulus observed for individual carbon nanotubes. *Nature*, *381*, 678–680. https://doi.org/10.1038/381678a0

Wang, G., Hu, X., Wu, X., & Li, Z. (2014). Sensors and Actuators B : Chemical Quantum dots-based glucose sensing through fluorescence quenching by bienzyme-catalyzed chromogenic substrate oxidation. *Sensors & Actuators: B. Chemical*, *205*, 61–66. https://doi.org/10.1016/j.snb.2014.08.053

Wang, H., Sun, C., Chen, X., Zhang, Y., Colvin, V. L., Rice, Q., Seo, J., Feng, S., Wang, S., & Yu, W. W. (2017). Excitation wavelength independent visible color emission of carbon dots. *Nanoscale*, *9*, 1909–1915. https://doi.org/10.1039/c6nr09200d

Wang, Y., & Hu, A. (2014). Carbon quantum dots: synthesis, properties and applications. *Journal of Materials Chemistry C*, *2*, 6921–6939. https://doi.org/10.1039/c4tc00988f

Wei, Y., Gao, C., Meng, F. L., Li, H. H., Wang, L., Liu, J. H., & Huang, X. J. (2012). SnO 2/reduced graphene oxide nanocomposite for the simultaneous electrochemical detection of cadmium(II), lead(II), copper(II), and mercury(II): An interesting favorable mutual interference. *Journal of Physical Chemistry C*, *116*(1), 1034–1041. https://doi.org/10.1021/jp209805c

Xiao, J., Liu, P., Li, L., & Yang, G. (2015). Fluorescence origin of nanodiamonds. *Journal of Physical Chemistry C*, *119*(4), 2239–2248. https://doi.org/10.1021/jp512188x

Xiao, J., Liu, P., & Yang, G. W. (2015). Nanodiamonds from coal under ambient conditions. *Nanoscale*, *7*(14), 6114–6125. https://doi.org/10.1039/c4nr06186a

Xu, Y., Wang, S., Hou, X., Sun, Z., Jiang, Y., Dong, Z., Tao, Q., Man, J., & Cao, Y. (2018). Coal-derived Nitrogen, Phosphorus and Sulfur Co-doped Graphene Quantum Dots: A Promising Ion Fluorescent Probe. *Applied Surface Science*, *445*, 519–526. https://doi.org/10.1016/j.apsusc.2018.03.156

Yahyazadeh, E., & Shemirani, F. (2019). Easily synthesized carbon dots for determination of mercury(II)in water samples. *Heliyon*, *5*(5), e01596. https://doi.org/10.1016/j.heliyon.2019.e01596

Yang, P., Zhu, Z., Zhang, W., Zhang, T., Li, X., Luo, M., Chen, W., Chen, M., & Zhou, X. (2020). Fluorescence mechanism of xylan-derived carbon dots: Toward investigation on excitation-related emission behaviors. *Journal of Luminescence*, *223*(December 2019), 117199. https://doi.org/10.1016/j.jlumin.2020.117199

Ye, R., Peng, Z., Metzger, A., Lin, J., Mann, J. A., Huang, K., Xiang, C., Fan, X., Samuel, E. L. G., Alemany, L. B., & Mart, A. A. (2015). Bandgap Engineering of Coal-Derived Graphene Quantum Dots. *ACS Applied Materials & Interfaces*, *7*, 7041−7048. https://doi.org/10.1021/acsami.5b01419

Ye, R., Xiang, C., Lin, J., Peng, Z., Huang, K., Yan, Z., Cook, N. P., Samuel, E. L. G., Hwang, C. C., Ruan, G., Ceriotti, G., Raji, A. R. O., Martí, A. A., & Tour, J. M. (2013). Coal as an abundant source of graphene quantum dots. *Nature Communications*, *4*, 2943. https://doi.org/10.1038/ncomms3943

Yi, Y., Deng, J., Zhang, Y., Li, H., & Yao, S. (2013). Label-free Si quantum dots as photoluminescence probes for glucose detection. *Chemical Communications*, *49*(6), 612–614. https://doi.org/10.1039/c2cc36282a

Yijie, W., Lei, W., & Haiyu, W. (2020). Investigation on the Relationship Between Carbon Cores and Fluorescence Moieties by Measurement of Fluorescence Anisotropy of CDs with Different Sizes. *Chemical Research in Chinese Universities*, *36*, 894–900. https://doi.org/10.1007/s40242-020-9109-2

Yoo, E., & Lee, S. (2010). Glucose Biosensors: An Overview of Use in Clinical Practice. *Sensors*, *10*, 4558–4576. https://doi.org/10.3390/s100504558

Zeinu, K. M., Hou, H., Liu, B., Yuan, X., Huang, L., Zhu, X., Hu, J., Yang, J., Liang, S., & Wu, X. (2016). A novel hollow sphere bismuth oxide doped mesoporous carbon nanocomposite material derived from sustainable biomass for picomolar

electrochemical detection of lead and cadmium. *Journal of Materials Chemistry A*, *4*(36), 13967–13979. https://doi.org/10.1039/c6ta04881a

Zhang, P., Zhao, X., Ji, Y., Ouyang, Z., Wen, X., Li, J., Su, Z., & Wei, G. (2015). Electrospinning graphene quantum dots into a nanofibrous membrane for dual-purpose fluorescent and electrochemical biosensors. *Journal of Materials Chemistry B*, *3*(12), 2487–2496. https://doi.org/10.1039/c4tb02092h

Zhang, W., Du, Y., & Wang, M. L. (2015). Sensing and Bio-Sensing Research Noninvasive glucose monitoring using saliva nano-biosensor. *SENSING AND Bio-Sensing Research*, *4*, 23–29. https://doi.org/10.1016/j.sbsr.2015.02.002

Zhang, W., Jiang, S., Hardacre, C., Goodrich, P., Wang, K., Shao, H., & Wu, Z. (2015). A Combined Raman Spectroscopic and Thermogravimetric Analysis Study on Oxidation of Coal with Different Ranks. *Journal of Analytical Methods in Chemistry*, *2015*, 306874. https://doi.org/10.1155/2015/306874

Zhang, Y., Li, K., Ren, S., Dang, Y., Liu, G., Zhang, R., Zhang, K., Long, X., & Jia, K. (2019). Coal-Derived Graphene Quantum Dots Produced by Ultrasonic Physical Tailoring and Their Capacity for Cu(II) Detection [Research-article]. *ACS Sustainable Chemistry and Engineering*, *7*, 9793–9799. https://doi.org/10.1021/acssuschemeng.8b06792

Zhao, S. X., Ta, N., & Wang, X. D. (2017). Effect of temperature on the structural and physicochemical properties of biochar with apple tree branches as feedstock material. *Energies*, *10*(9). https://doi.org/10.3390/en10091293

Zhiguo Sun, Xiaoming Li, Ye Wu, Changting Wei, H. Z. (2018). Green luminescence origin of carbon quantum dots: specific luminescence bands originate from oxidized carbon groups. *New Journal of Chemistry*, *42*, 4603–4611. https://doi.org/10.1039/C7NJ04562J

Zhou, Q., Zhao, Z., Zhang, Y., Meng, B., Zhou, A., & Qiu, J. (2012). Graphene sheets from graphitized anthracite coal: Preparation, decoration, and application. *Energy and Fuels*, *26*(8), 5186–5192. https://doi.org/10.1021/ef300919d

Zhu, L., Tian, C., Yang, R., & Zhai, J. (2008). Anodic stripping voltammetric determination of lead in tap water at an ordered mesoporous carbon/nafion composite film electrode. *Electroanalysis*, *20*(5), 527–533. https://doi.org/10.1002/elan.200704088

LIST OF PUBLICATIONS

Journal Publications

1. **Ashlin M. Raj**, Manoj Balachandran. (2021) Cost-effective route to nanodiamond from low-rank coal and their fluorescent & dielectric characteristics. *Ceramics International*, 79(1) 887-895. https://doi.org/10.1016/j.ceramint.2021.09.171 (Impact factor – 4.527)
2. **Ashlin M. Raj**, Manoj Balachandran. (2020) Coal-Based Fluorescent Zero-Dimensional Carbon Nanomaterials: A Short Review. *Energy & Fuels* 2020 *34* (11),13291-13306. https://dx.doi.org/10.1021/acs.energyfuels.0c02619 (Impact factor – 3.605)
3. Manoj Balachandran, **Ashlin M. Raj**, & George Thomas. (2018) Tailoring of low-grade coal to fluorescent nanocarbon structures and their potential as a glucose sensor. *Scientific Reports* 8, 13891. https://doi.org/10.1038/s41598-018-32371-9 (Impact factor – 4.379)
4. Manoj Balachandran, **Ashlin M. Raj**, & George Thomas. (2018) Facile synthesis of preformed mixed nano-carbon structure from low rank coal. Materials Science-Poland 36(1):14-20. DOI: 10.1515/msp-2018-0026 (Impact factor – 0.95)
5. Manoj Balachandran, **Ashlin M. Raj**, & George Thomas. (2017) Tunable direct band gap photoluminescent organic semiconducting nanoparticles from lignite. *Scientific Reports* 7, 18012. https://doi.org/10.1038/s41598-017-18338-2 (Impact factor – 4.379)
6. Manoj Balachandran, **Ashlin M Raj,** (2017) Extraction and Characterization of Preformed Mixed phase Graphene Sheets from Graphitized Sub-Bituminous Coal. *Asian Journal of Chemistry* 29 (11), 2425-2428. https://doi.org/10.14233/ajchem.2017.20722 (SJR – 0.15)

Manuscripts communicated

1. **Ashlin M. Raj**, Manoj Balachandran. Low-grade coal-derived carbon nanostructures as a sensitive fluorescence probe for micromolar glucose detection (Communicated to Sensors and Actuators B: Chemical).
2. **Ashlin M. Raj**, Manoj Balachandran. Exploration of the potential efficacy of lignite derived carbon nanostructure for the simultaneous electrochemical detection of cadmium (II) and lead (II) (Communicated to Environmental Pollution)**.**

Patent communicated

Ashlin M Raj, Manoj Balachandran. Low cost lignite derived mesoporous nanocarbon for simultaneous electrochemical detection of heavy metal ions cadmium and lead

LIST OF CONFERENCES AND WORKSHOPS ATTENDED

1. International Conference on Physics of Materials & Nanotechnology, 19-21 September 2019, Department of Studies in Physics, Mangalore University.
2. National Conference on Nanomaterials and Nanoelectronic Devices for Energy Applications, 28 -29 July 2017, Indian Association of Physics Teachers (IAPT).
3. Capacity Enhancement Workshop on Intellectual Property Rights (IPR), 27-28 March 2017, Centre for Education Beyond Curriculum (CEDBEC).
4. ACS on Campus India Virtual Event, 10th August 2020, ACS
5. Characterization of 2D Materials with Atomic Force Microscopy, 19th August 2020, Oxford Instruments, Asylum Research.